

UCLA

UCLA Electronic Theses and Dissertations

Title

Growth of MoS₂ Layers by Two-Step Chemical Vapor Deposition

Permalink

<https://escholarship.org/uc/item/0249b3sk>

Author

Sheu, An-Di

Publication Date

2015

Peer reviewed|Thesis/dissertation

UNIVERSITY OF CALIFORNIA

Los Angeles

Growth of MoS₂ Layers by
Two-Step Chemical Vapor Deposition

A thesis submitted in partial satisfaction
of the requirements for the degree Master of Science
in Materials Science and Engineering

by

An-Di Sheu

2015

© Copyright by

An-Di Sheu

2015

ABSTRACT OF THE THESIS

Growth of MoS₂ Layers by Two-Step Chemical Vapor Deposition

by

An-Di Sheu

Master of Science in Materials Science and Engineering

University of California, Los Angeles, 2015

Professor Suneel Kodambaka, Chair

Monolayer molybdenum disulfide (MoS₂), a two-dimensional (2D) crystal with a direct bandgap, is a promising candidate for nano electronic devices, energy storage, and photocatalysts. People are researching for large-area single-layer MoS₂ growth. In my work, I investigated the growth of monolayer MoS₂ on SiO₂/Si substrate by chemical vapor deposition (CVD). Using sulfur and molybdenum trioxide (MoO₃) as precursors to grow 2D MoS₂ in the tube furnace CVD system. As part of my thesis, I carried out several growth experiments while varying the deposition parameters. The as-grown samples are characterized using optical, scanning electron, and atomic force microscopes and Raman spectroscopy. I have also developed

a two-step approach to grow MoS₂ layers. This new approach has great potential to grow large-area single-layer MoS₂.

The thesis of An-Di Sheu is approved.

Yang Yang

Yu Huang

Suneel Kodambaka, Committee Chair

University of California, Los Angeles

2015

Table of Contents

Chapter 1. Introduction	1
1.1 Two-Dimensional Layered Materials	1
1.2 2D Transition-Metal Dichalcogenides	2
1.3 Application of Single Layer MoS ₂	4
1.4 Synthesis of Single Layer MoS ₂	6
1.4.1 Exfoliation	7
1.4.2 Chemical Vapor Deposition	8
1.4.3 CVD of MoS ₂ using MoO ₃ or MoCl ₅ as the Precursor	8
1.4.4 CVD of MoS ₂ using (NH ₄) ₂ MoS ₄ as the Precursor	8
1.4.5 CVD of MoS ₂ using Mo Metal and S Powder as the Precursors	9
1.4.6 Vapor Phase Deposition of MoS ₂ via Thermal Evaporation	9
1.4.7 Deposition of MoS ₂ via Magnetron Sputtering	9
Chapter 2. Experimental	12
2.1 2D Layered MoS ₂ Growth	12
2.2 Sample Characterization	14
2.2.1 Raman Spectroscopy	14
2.2.2 Scanning Electron Microscopy	18
2.2.3 Atomic Force Microscopy	19

Chapter 3. Results and Discussion	21
3.1 Effect of Temperature	22
3.2 Effect of Precursor Pressure and Flow Rate	23
3.3 2D Layered MoS ₂ Growth with Different Amounts of Precursors	32
3.4 Observation of Site-Specific Morphologies	34
3.5 Two-Step 2D Layered MoS ₂ Growth	36
3.6 Discussion	44
Chapter 4. Conclusion	46
References	49

Acknowledgments

First of all, I would like to express gratitude to my advisor Prof. Kodambaka for the support in the past two years. His keen insight, creative idea and knowledge related to my research helped me a lot to finish my thesis. Besides, I am so grateful to be one of the members in Kodambaka's group. Dr. Abbas Ebnouassir and Dr. Chilan Ngo spent so much time teaching me Raman spectroscopy, AFM, and TEM. Without their help I could not have all these great images and data in my thesis. I would also like to give thanks to Dian Yu, Pedro Arias, Josh Fankhauser, and Hong-yang Li. I really enjoy working with them and miss all the hilarious moments in our lab. I cannot survive without their spiritual support. Last but not the least, I would like to express appreciation to my family, my girlfriend, and all the friends who care about me. Thanks for their full support in my life.

Chapter 1: Introduction

1.1 Two-Dimensional Layered Materials

Since the discovery of graphene in 2004 [1], two-dimensional (2D) layered materials have drawn a lot of attention from materials scientists. With fascinating unusual properties, 2D layered materials could be used in field-effect transistors [2], photosensors [3], photovoltaics [4], ultracapacitors [5], composite materials [6], and photocatalysts [7]. 2D layered materials typically have strong in-plane bonds and weak van der Waals bonds between the layers. Interestingly, physical, chemical, and mechanical properties of these materials vary with the thickness. For instance, graphene is the strongest materials ever discovered with tensile strength of 130 gigapascals, compared to 0.4 gigapascals for A36 structural steel [8]. In contrast, graphite is very brittle due to its weak interlayer bonding. Graphene is also an excellent conductor of heat (heat conductivities: $2000 - 4000 \text{ W m}^{-1} \text{ K}^{-1}$) and electricity (electronic mobility: $200,000 \text{ cm}^2 \cdot \text{V}^{-1} \text{ s}^{-1}$) with ballistic transport [9]. However, the thermal and electronic conductivities of graphite are very anisotropic: phonons and electrons travel much more easily along the layer than across the layers. Despite all these attractive characteristics, the use of graphene in electronics has been limited because most of the electronic applications require a bandgap, which does not exist in graphene [10]. Researchers tried to introduce a bandgap in graphene by synthesizing graphene nano-ribbons but carrier mobility in the nano-ribbons is low [10]. This and other unsuccessful attempts to engineer its bandgap motivated researchers to focus on other 2D layered materials, which have bandgaps. Hexagonal

boron nitride (h-BN) and molybdenum disulfide (MoS_2) are two of the most studied 2D layered materials after graphene.

1.2 2D Transition-Metal Dichalcogenides

Transition-metal dichalcogenides (TMDCs) of the form MX_2 are produced by combining the transition-metals ($\text{M} = \text{Ti}, \text{Zr}, \text{Hf}, \text{V}, \text{Nb}, \text{Ta}, \text{Mo}, \text{W}, \text{Pt}$) with the chalcogens ($\text{X} = \text{S}, \text{Se}, \text{Te}$) in the form of MX_2 [7,11]. The transition-metal atoms are sandwiched between two layers of chalcogen atoms. Bulk TMDCs are multiple layers of TMDCs stacked together by van der Waals forces. One transition-metal atom is

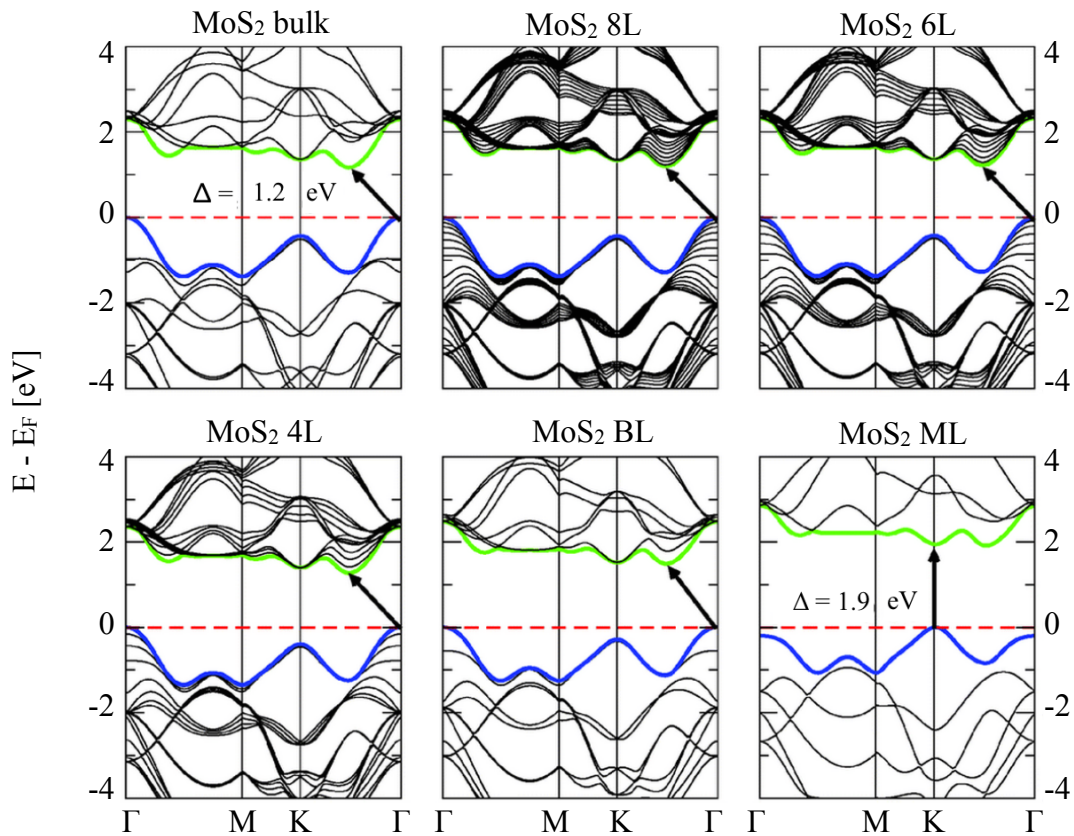


Figure 1. Calculated band structure of MoS_2 . The bandgap of MoS_2 decreases with the increasing number of MoS_2 layer. The bandgap in bulk MoS_2 is indirect while the bandgap in monolayer MoS_2 is direct [12].

surrounded by six chalcogen atoms to form trigonal prismatic structure [11]. Among the TMDCs, MoS₂ and related alloys have been widely used as solid lubricant [13]. Similar to graphene, TMDCs also possess thickness-dependent properties [14,15]. In case of MoS₂, there is a change of bandgap from indirect to direct with decreasing number of layers [16], see figure 1. TMDCs composed of Mo or W are semiconductors and that is the reason why they are investigated more than other TMDCs. The lattice constants and bandgaps of Mo and W based dichalcogenides are listed in Table 1 [17-19], which shows that they are semiconductors. Other TMDCs such as TiSe₂ and NbS₂ are semimetals [11].

The Mo and W based TMDCs usually crystallize in three different structures: 2H, 3R, and 1T [20]. The difference in stacking between the layers for these structures are shown in figure 2. 2H is the most common and stable phase among these three. 1T is a metastable phase, which provides lower contact resistance and could be synthesized by lithium intercalation [21]. To date, the electronic properties of 3R phase remain largely unexplored. Both 1T and 3R phases can change to 2H structure through heating.

TMDC	MoS ₂	MoSe ₂	MoTe ₂	WS ₂	WSe ₂	WTe ₂
Lattice constant	3.11 Å	3.24 Å	3.46 Å	3.13 Å	3.25 Å	3.47 Å
Bandgap (bulk)	1.23 eV	1.09 eV	1.0 eV	1.35 eV	1.20 eV	0.8 eV
Bandgap (monolayer)	1.87 eV	1.62 eV	1.25 eV	1.98 eV	1.68 eV	1.24 eV

Table 1. Lattice constants and bandgaps of Mo and W based TMDCs [17-19]

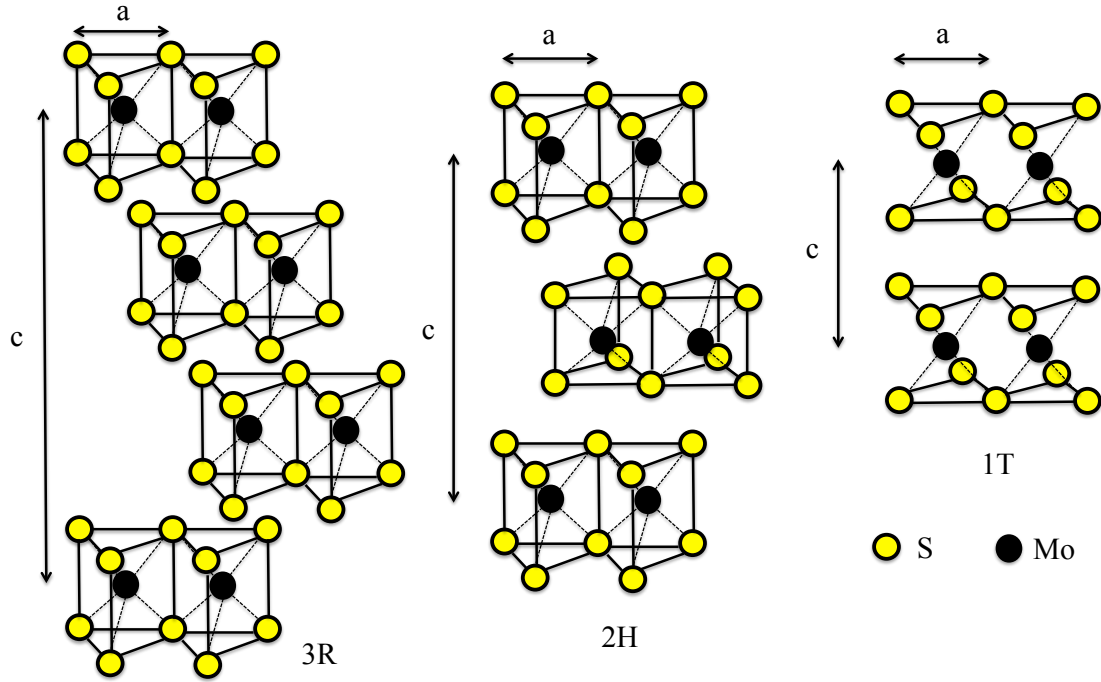


Figure 2. Three different kinds of stacking between layers resulting in different phases: 3R, 2H, and 1T. a and c are the in-plane and out-of-plane lattice constants, which for 2H-structured MoS_2 are 3.1 \AA and 12.3 \AA respectively.

1.3 Applications of Single Layer MoS_2

The 2D nature of monolayer MoS_2 leads to quantum confinement [22], high absorption coefficient [4], and efficient electron-hole pair generation [4] under photo-excitation. Due to the fact that TMDCs are vertically held together by van der Waals forces the lattice mismatch between the layers of different TMDCs is not a problem for the fabrication of vertical heterostructures. Also the lattice constants of the TMDCs (see Table 1) are very close. Therefore, it is possible to build vertical, lateral, and alloy heterostructures. Such TMDC heterostructures with dissimilar bandgaps have applications such as photocatalysts [23], photodetectors [24], and field-effect transistors [25].

Single layer MoS₂ has great potential in electronic devices because of its high on/off ratio ($\sim 10^8$) [2]. Scientists have used single layer MoS₂ to fabricate ultra-thin field-effect transistors. Additionally, in contrast to graphene, monolayer MoS₂ has a direct bandgap of 1.8 eV, which is highly desirable for switching on and off. As mentioned earlier, the 2H and 1T phases in MoS₂ have different contact resistances. Scientists have utilized this resistance difference to build field-effect transistor [21]. The 1T phase is in contact with source and drain to provide better conductance and the 2H phase is in contact with gate to avoid leakage current.

Monolayer MoS₂ has also been used to fabricate photodetectors. Because monolayer MoS₂ is a direct bandgap semiconductor, it could be good for optoelectronic devices. The direct bandgap provides a high absorption coefficient and efficient electron-hole pair generation. The high photoresponsivity (880 AW^{-1}) is 10^3 times superior to the best graphene photodetector [3]. The ability to grow large-area MoS₂ layers can facilitate the development of flexible and high-sensitivity MoS₂ optoelectronic devices.

Monolayer MoS₂ is also a good photocatalyst for water splitting. TiO₂ nanocrystals grown in the presence of a layered MoS₂ hybrid are found to be high-performance photocatalysts for H₂ evolution [26]. Single-layer MoS₂ by itself was also reported as an efficient photocatalyst based on first-principles calculations [11,27]. There are three criteria to become a promising semiconductor for water splitting. First, the bandgap has to be larger than 1.6-1.7 eV to drive the kinetics of hydrogen evolution reaction. Second, the band edges must straddle the redox potentials of water. Last, the semiconductor should be insoluble in water. Fortunately, monolayer MoS₂ meets all the three criteria.

The highly flexible and transparent MoS₂ based field-effect transistor could also be used as biosensors for various biomarkers. It is able to detect cancer marker proteins [28] and pH variation [29]. The biosensor should meet criteria such as high detection speed, high sensitivity, low cost, and versatility. MoS₂ based FETs has higher on/off ratio ($\sim 10^8$) than graphene based FETs and this is the main reason why MoS₂ based FETs are more suitable as biosensors.

Another promising application of MoS₂ is as anode in lithium ion batteries. The conventional lithium ion batteries utilize graphite as the anode. The theoretical capacity for graphite is low (372 mA h/g). Higher capacity materials such as Si (4200 mA h/g) and Sn (994 mA h/g) have poor cycling characteristic. However, they suffer from large volume changes when charging and discharging. The weak van der Waals bondings between MoS₂ layers allow Li⁺ ions to diffuse in and out without a significant increase in volume expansion. The capacity of exfoliated MoS₂ could be maintained above 500 mA h/g after 50 cycles [30]. MoS₂ is also reported as an excellent supercapacitor. 2D layered MoS₂ based micro-supercapacitors with a high area capacitance of 8 mF cm⁻² and good cycle performance are superior to graphene based micro-supercapacitors [31]. People have demonstrated a low-cost spray painting process and subsequent laser patterning to fabricate the MoS₂ micro-supercapacitors [31].

1.4 Synthesis of Single Layer MoS₂

Single Layer MoS₂ can be synthesized using a variety of methods. We can classify all the methods into two main categories, top-down and bottom-up approaches. Top-down methods typically involve mechanical, solution phase, or chemical exfoliation

of single and few layers from the bulk. Most commonly employed bottom-up approaches include chemical and physical vapor deposition (CVD and PVD) of MoS₂ layers.

1.4.1 Exfoliation

The first free standing graphene layers were obtained by mechanical exfoliation [1]. This method involves repeated peeling of individual graphene layers from highly oriented pyrolytic graphite with scotch tape. Since then mechanical exfoliation has been widely used for 2D layered material synthesis. 2D layers can also be produced in large amount by non-chemical, solution-phase exfoliation from their bulk counterparts [32]. This method is attractive for the deposition of 2D layered materials on a variety of substrates. Besides liquid exfoliation, people have tried exfoliation by chemical reactions involving the intercalant [33], thermal shock [34], and acid treatment [35]. However, these methods may not be ideal for the production of 2D layered materials for all the applications because the 2D layered materials produced by chemical exfoliation usually react with the solvent resulting in undesirable compositions and structures.

Until now, none of the above-mentioned top-down methods have been used for mass production because the yield rate and the reproducibility are low. In order to make 2D layered materials for commercial applications, we need to figure out ways other than exfoliation to synthesize large area 2D layered materials with desired composition and structure.

For the synthesis of MoS₂ layers, bottom-up approaches include deposition using solid, liquid, and vapor precursors. CVD usually involves precursors reacting with each other and the reaction product deposited on the substrate. PVD usually involves

generation and vapor phase transport of solid materials by heat, plasma, or pulsed laser and deposition of the condensate as a thin film on the substrate.

1.4.2 Chemical Vapor Deposition (CVD)

In this approach, a substrate is exposed to one or more volatile precursors, which react with each other and the reaction product is deposited on the substrate. The undesired byproducts are usually removed from reaction chamber by carrier gas using pumps. CVD systems could operate at various pressures, atmospheric pressure (or above), low vacuum ($\sim 10^{-3}$ Torr), or ultrahigh vacuum ($10^{-6} \sim 10^{-8}$ Torr). MoS₂ thin films have been grown via CVD using a variety of Mo precursors, such as Mo film, MoCl₅, MoO₃, and solid S or H₂S gas. Thermal decomposition of single precursor such as (NH₄)₂MoS₄ has also been shown to yield MoS₂ layers..

1.4.3 CVD of MoS₂ using MoO₃ or MoCl₅ as the Precursor

In this approach, solid MoO₃ or MoCl₅ typically in the form of powders are vaporized and converted to MoS₂ by reacting with S vapor at high temperatures (> 800 °C). MoO₃ or MoCl₅ are placed at the hottest zone (T > 800 °C) of the furnace to vaporize them. Sulfur vapor is introduced into the system by heating sulfur powder and carrying the vapor with Ar flow. The precursors would react to produce MoS₂, which is subsequently deposited on the substrate [36].

1.4.4 CVD of MoS₂ using (NH₄)₂MoS₄ as the Precursor

Thermolysis of ammonium thiomolybdates [(NH₄)₂MoS₄] in a N₂ environment is known to result in the conversion of (NH₄)₂MoS₄ to MoS₃ at 120~360 °C [37]. The subsequent conversion of MoS₃ to MoS₂ requires a higher temperature (> 800 °C). It was also reported that the conversion of (NH₄)₂MoS₄ to MoS₂ in the presence of H₂ occurs at a lower temperature (425 °C) [38]. However, MoS₂ decomposes into Mo in

the H₂ environment at over 500 °C. A variation of this approach involves two steps. First, the substrate is dip-coated with (NH₄)₂MoS₄ in solution and the substrate is then heated in Ar/H₂ environment at 500 °C. To obtain better crystallinity, people annealed the sample in Ar/S atmosphere at 1000 °C or higher to form MoS₂ [38].

1.4.5 CVD of MoS₂ using Mo Metal and S Powder as the Precursors

MoS₂ layers have also been synthesized via sulfurization of Mo thin films. In this approach a thin film of Mo (1-5 nm thick) is first deposited on a substrate by evaporation or sputtering. The Mo films are then exposed to sulfur vapor at high temperature (750 °C) forming very thin MoS₂ layers [39].

1.4.6 Vapor Phase Deposition of MoS₂ via Thermal Evaporation

Direct thermal evaporation of MoS₂ has been shown to yield MoS₂ thin films. MoS₂ powder is first pressed into tablets and sintered for 20 min at 300 °C. The MoS₂ tablet is then placed in a closed box with pinholes. These pinholes could make the MoS₂ flow rate small enough to grow MoS₂ thin film. The reactive chamber is set at 500 °C with Ar as the carrier gas to bring MoS₂ vapor to the substrate [40].

1.4.7 Deposition of MoS₂ via Magnetron Sputtering

Magnetron sputtering was reported as a one-step process to synthesize monolayer MoS₂ at wafer scale. Initial base pressure is maintained at about 2.25×10^{-7} Torr to minimize impurities in the chamber. The Ar pressure is fixed at 4.5×10^{-4} Torr. MoS₂ films are grown at high temperature (> 700 °C) using Mo metal target sputtered in vaporized sulfur ambient. Sulfur is vaporized using heating tape. The sputtering power is maintained low to facilitate slow growth of MoS₂ thin films [41].

Each of the synthesis methods mentioned above have certain advantages and

disadvantages. For example, the MoS₂ sample grown using (NH₄)₂MoS₄ as the precursor involves many steps. First, (NH₄)₂MoS₄ converts to MoS₃ at 120~360 °C. Second, MoS₃ decomposes into MoS₂ at 800 °C. Last the MoS₂ sample requires further annealing at 1000 °C in an inert gas to improve its crystallinity [38]. Furthermore, (NH₄)₂MoS₄ is synthesized by dissolving (NH₄)₆Mo₇O₂₄*4H₂O in ammonia solution (25%wt) and introducing H₂S to this solution [42]. To obtain highly crystallized MoS₂ with (NH₄)₂MoS₄ there are so many steps involved.

MoS₂ synthesized by e-beam evaporated Mo thin film and sulfurized in sulfur vapor at 750 °C is typically polycrystalline and the thickness of the film is not uniform. The grain size of MoS₂ synthesized by evaporated Mo is typically smaller (< 1 μm) than the counterpart synthesized by CVD using MoO₃ and sulfur as precursors. The smaller grain size imply more grain boundaries, which leads to more electron scattering within MoS₂.

The thinnest MoS₂ thin film ever reported grown by thermal evaporation was quite thick (a few atomic layer to 10 nm thick) in comparison to other techniques. We can grow high quality MoS₂ thin films using MoCl₅ as a precursor but MoCl₅ is an aggressive oxidant and readily hydrolyzes to release HCl. HCl is a strong acid which could be dangerous. Among all the synthesis methods mentioned above, using MoO₃ powder and sulfur powder as the precursors has many advantages. MoO₃ has low melting point (T_M = 795 °C) and high vapor pressure (10⁻¹ Torr at T = 703 °C) [43]. Using this method, monolayer single domain MoS₂ with very good electrical and photoelectric properties has been grown [40].

Researchers have synthesized MoS₂ layers at different temperatures (650 °C - 850

°C) [44,45], different pressures (low vacuum to over atmospheric pressures) [44,45] and on patterned and seeded substrates [46]. However, the growth mechanism is still not well-established. Only a few papers discuss the growth mechanism and the factors contributing to the growth of large-area single-layer MoS₂ in such conditions. Most of the literatures do not discuss the effect of growth parameters.

My thesis focused on the growth of MoS₂ and investigated the effect of parameters, including growth temperature, chamber pressure, precursor amount, and location of the substrate as a means to develop a better understanding of the MoS₂ layer growth mechanism.

Chapter 2: Experimental

2.1 2D Layered MoS₂ Growth

All of my growth experiments are carried out in a tube furnace. Figure 3 is a schematic of my CVD system. The temperatures of substrates and precursors, carrier gas flow rate, total pressure, and the amount of precursors could all be controlled independently in this system. The growth precursors and the samples are placed in a 1-inch diameter and 2.5 feet long quartz tube, which is surrounded by the furnace. One end of the tube is connected to a series of gas inlets through which gases such as argon (Ar), nitrogen (N₂), and oxygen (O₂) can be introduced into the system. The other end of the tube is connected to a mechanical pump. All of my MoS₂ synthesis experiments were carried out using Si(001) substrates covered with 300 nm thick SiO₂ (MTI Corporation©). The substrates were cleaned first with acetone and then with deionized water for 10 and 5 minutes, respectively. Then substrates were placed on top of a boat shaped aluminum oxide crucible (1 cm in diameter) as shown in the figure 3. A crucible containing MoO₃ powder (Alfa Aesar© 99.5%) was placed inside the aluminum oxide boat at the hottest zone (700 ~ 850 °C) of the tube and another

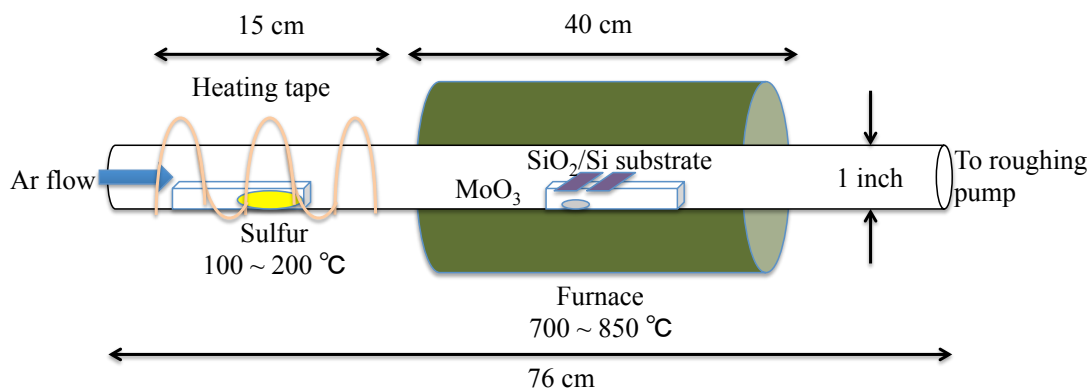


Figure 3. Schematic of tube furnace system.

crucible containing sulfur powder (Sigma-Aldrich© 99.9%) was placed at the upstream of the quartz tube. After both precursors and substrates were loaded into the tube, 50 ~ 200 sccm of Ar gas (Airgas© 99.995%), controlled by mass flow controller, was introduced into the tube to purge the system. Then the pump end of the tube was closed in order to maintain a high Ar pressure in the system. The base pressure before Ar purging is 0.03 Torr and after one hour Ar purging the pressure is around 100 Torr. One hour after pumping to 0.03 Torr, the furnace temperature is increased to simultaneously vaporize MoO₃ and heat the substrate. When the temperature of the MoO₃ reaches target temperature (700-800 °C), the sulfur powder is heated using the heating tape. Sulfur vapor is transferred to the center of the tube by Ar gas, where it reacts with MoO₃ to form MoS₂. The substrate temperature was set to 850 °C and the growth time is typically 10 to 15 minutes. After the growth, the outlet valve between the tube and the pump was opened to purge all the gases. The system was cooled to room temperature with continuous Ar flow (50 ~ 200 sccm) while the mechanical pump was running.

The Mo-S binary phase diagram [46] in figure 4 can help identify the deposition parameters favorable for the growth of MoS₂. From the phase diagram, it appears that stoichiometric, single-phase MoS₂ is best synthesized using S-rich conditions. The S to Mo ratio in my experiments is usually higher than 10 and the temperature is always higher than 700 °C. This growth condition is equivalent to the “MoS₂ + 1 atm gas” region. The need for this “1 atm gas” is supported by our experiments, where we grow MoS₂ at a higher pressure environment and will be discussed in Chapter 3.

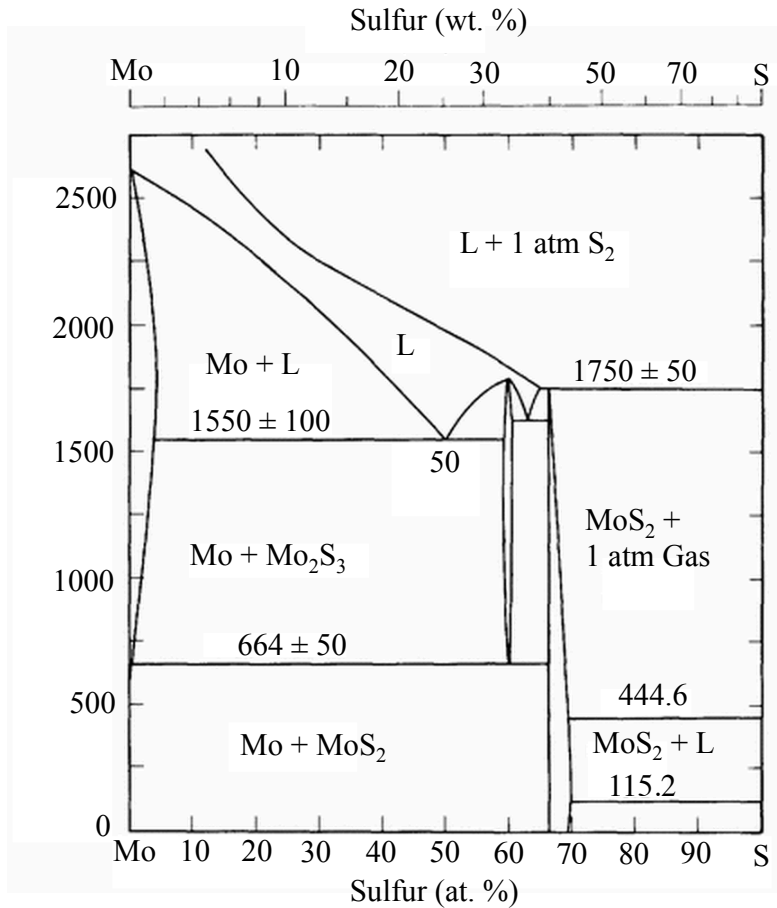


Figure 4. Mo-S binary phase diagram, from [47].

2.2 Sample Characterization

The as-grown MoS₂ samples were characterized using Raman spectroscopy (Renishaw InVia Raman Microscope) using laser wavelength $\lambda = 785, 633$ nm and a laser power of 1 mW, scanning electron microscopy (SEM)(FEI Nova nanoSEM 230), and atomic force microscopy (AFM)(Bruker Dimension FastScan Scanning Probe Microscope) in tapping mode.

2.2.1 Raman Spectroscopy

The phenomenon of Raman scattering is well-studied and it is beyond the scope of my thesis to present the details of this phenomenon and the measurement techniques. However, those interested in learning more about this topic may find more

information here [48,49] and elsewhere. Briefly, Raman spectroscopy provides information about molecular vibrations that can be used for sample identification. It is based on the inelastic scattering (Raman scattering) of monochromatic light such as laser. The laser beam scatters off mostly is unchanged in energy (Rayleigh scattering). Only a small fraction ($1/10,000,000$) of light loses or gains energy (Raman scattering) with the molecules of target materials. The CCD (charge coupled device) detectors are used for Raman spectroscopy because they are sensitive to light. They detect the frequency of light after scattering with the target materials. Each molecule has its own unique vibrational frequency. After the incoming light scattering with the molecules, the energy of light changes. The energy shift relates to the molecular vibrational

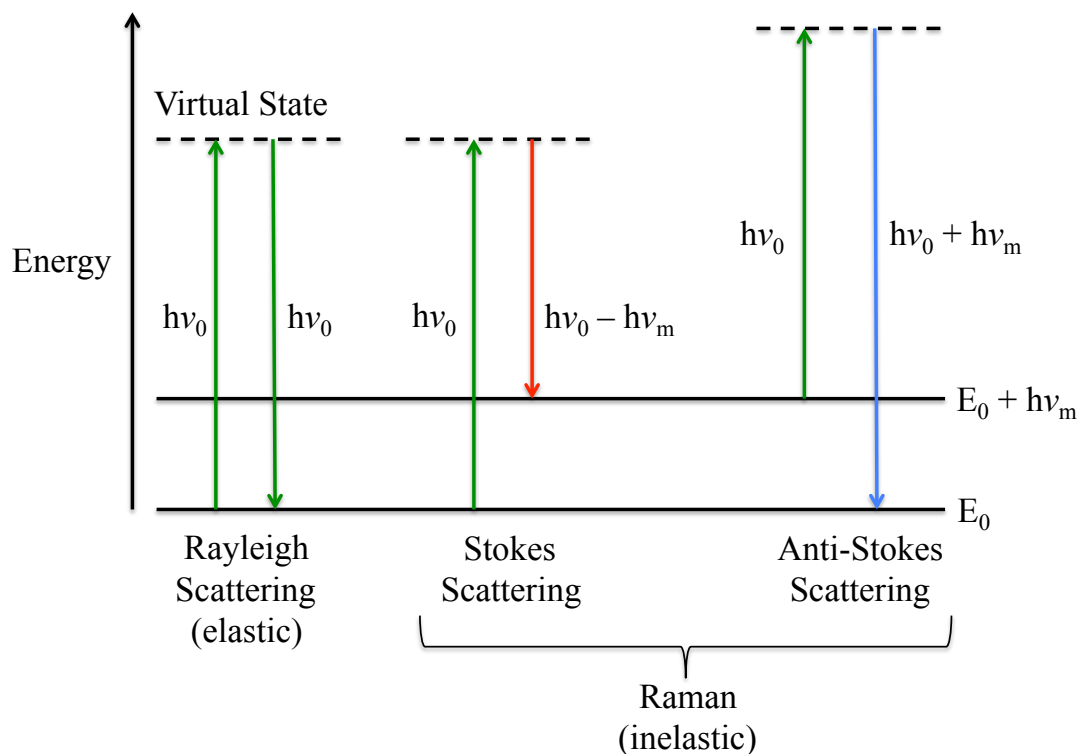


Figure 5. Energy-level diagram showing the energy change in Raman scattering and Rayleigh scattering. E_0 : ground state; $h\nu_m$: energy difference after scattering; $h\nu_0$: energy of incident beam [50].

frequency. The sample may absorb energy in which case the emitted photon has a lower energy than the absorbed photon. The outcome is known as Stokes scattering. The sample could lose energy to the incoming photon and the emitted photon has a higher energy than the absorbed photon. This outcome is called anti-Stokes scattering. If the incoming photon does not gain/lose energy, i.e. when the photon is elastically scattered, the process is called Rayleigh scattering. The energy level diagram of Rayleigh, Stokes, and anti-Stokes scattering are shown in figure 5. Stokes scattering is a more common result compared to anti-Stokes scattering due to the fact that there are

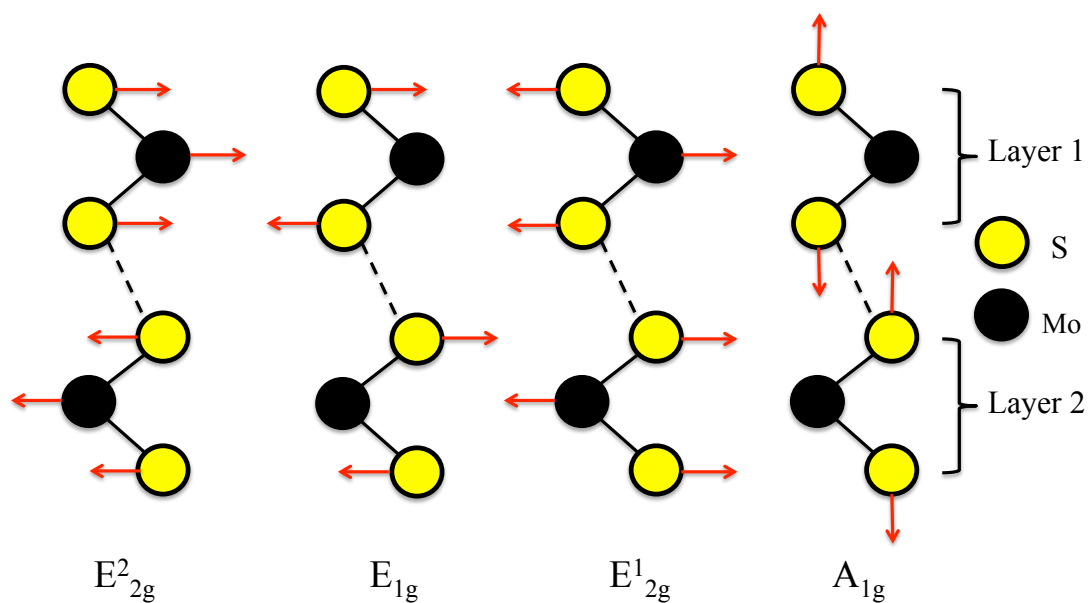


Figure 6. Four most common vibrational modes in MoS₂. The red arrows represent the atomic displacement during vibration. E_{2g}^1 represents the in-plane vibration mode observed at around 383 cm⁻¹ in Raman spectrum obtained using a laser $\lambda = 633$ nm. A_{1g} represents the interlayer vibration mode at around 409 cm⁻¹ in Raman spectrum. E_{2g}^2 cannot be detected because of the limited rejection of the Rayleigh scattered radiation. E_{1g} cannot be detected because of selection rules for our scattering geometry [51].

usually more molecules in the ground state at room temperature.

There are four Raman-active vibrational modes (E_{2g}^2 , E_{1g} , E_{2g}^1 , A_{1g}) in MoS_2 (figure 6). Using $\lambda = 633$ nm, I observed the E_{2g}^1 and A_{1g} modes near 400 cm^{-1} . The other two modes (E_{1g} , E_{2g}^2) are hard to detect [51]. E_{2g}^1 represents the in-plane vibrational mode, whereas A_{1g} is the interlayer vibrational mode and they are observed at around 383 cm^{-1} and 409 cm^{-1} respectively for bulk MoS_2 . The positions of both the peaks are related to the thickness of MoS_2 . For the given λ the distance between E_{2g}^1 and A_{1g} decreases with decreasing thickness of MoS_2 [51]. This shift in the peak positions is attributed to thickness-dependent suppression of atomic vibrations by the interlayer van der Waals forces in MoS_2 [51]. As demonstrated in figure 7, different number of layers in MoS_2 corresponds to different E_{2g}^1 and A_{1g} frequencies in Raman spectra [51]. The observed blue-shift (shifting to higher frequency) of A_{1g} peak with increasing layer number is consistent with the theoretical prediction [52]. Therefore, we can determine the number of layers in MoS_2 using Raman spectroscopy. An important factor to consider in characterization of MoS_2 using Raman spectroscopy, however, is the laser wavelength could influence the experiment results. MoS_2 is more sensitive to laser $\lambda = 633$ nm than 785 nm wavelength. We could barely detect single-layer MoS_2 with 785 nm laser but easily get the signal with 633 nm laser. This is due to the fact that the intensity of Raman scattering is proportional to the fourth power of source frequency. Hence, at the same laser energy, Raman signal obtained using $\lambda = 633$ nm is more intense than with the 785 nm.

In my thesis, I used Raman spectroscopy ($\lambda = 633$ nm) to confirm the existence of

MoS₂ and to determine the number of layers of MoS₂ thin film.

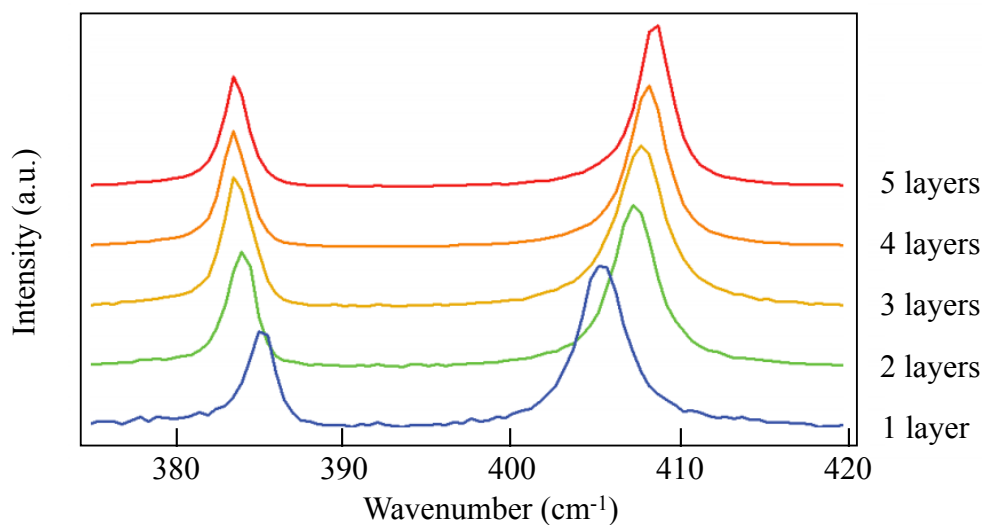


Figure 7. Raman spectra of MoS₂ in different number of layers. The peaks around 385 cm⁻¹ and around 405 cm⁻¹ correspond to the vibrational modes E_{2g}¹ and A_{1g}, respectively. The distance between E_{2g}¹ and A_{1g} increases as the number of layers increases [53].

2.2.2 Scanning Electron Microscopy

For a detailed description of operating principles and applications of scanning electron microscopy (SEM), please see [54]. Briefly, SEM utilizes a focused high energy (~ 0.2 to 30 kV) electron beam to scan the specimen and to generate a variety of signals at the surfaces of solid specimens. The different signals come from the different interactions between electrons and specimens. Secondary electrons, backscattered electrons, and characteristic X-rays are three of the most common signals used in the SEM for materials characterization. Secondary electrons are usually used for the determination of morphology and topography of the samples while backscattered electrons are valuable for illustrating compositional contrast in

multiphase samples. Characteristic X-rays are generated by the inelastic collision between incident electrons and electrons in samples providing the elemental composition of the samples. SEM is one of the best ways to visualize the topography at high resolution (~ 1 nm). As part of my thesis, I have used SEM to study the morphology and the distribution of MoS₂ triangles and films on SiO₂/Si substrates. I used the secondary electron mode to observe and characterize the triangles. I have determined the shapes of MoS₂ islands and also measured the size and density of the triangles. The size of the triangles in my experiments vary from 5 μm to 50 μm depending on the growth parameters. Energy-dispersive X-ray spectroscopy (EDS), commonly used to determine sample composition in the SEM, was not used in my experiments because the EDS peaks for Mo ($L\alpha = 2.29$ keV) and S ($K\alpha = 2.31$ keV) overlap making it difficult to quantify the Mo and S contents in the samples.

2.2.3 Atomic Force Microscopy

Atomic force microscopy (AFM) is a surface characterization technique used for high-resolution imaging of surfaces and measurement of surface topography. For a detailed description of AFM, its variants, and applications, please see [55]. The relevant surface topographical information is gathered by a mechanical probe “touching” the surface. The AFM consists of a cantilever with a very sharp tip used to scan the sample surface. When the tip is brought very close to the surface, there is a force between the tip and the surface resulting in deflection of the cantilever, which is used to determine the surface roughness. One of the main benefits of AFM, in contrast to a related surface characterization method, scanning tunneling microscopy (STM), is that it can be used to investigate electrically non-conductive materials. This feature facilitates characterization of our MoS₂ samples grown on SiO₂ substrates.

Using AFM, we can measure the thickness of the MoS₂ layer and estimate the number of layers within each MoS₂ triangle. Furthermore, we can compare the AFM data with Raman spectroscopy results to check if these two results agree with each other.

Chapter 3: Results and Discussion

In this chapter, I will present my results obtained from a series of growth experiments carried out at a function of deposition parameters. Table 2 shows representative scanning electron microscopy (SEM) images obtained from samples grown at various deposition parameters.

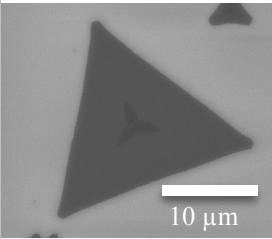
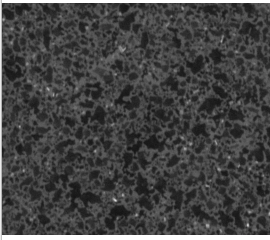
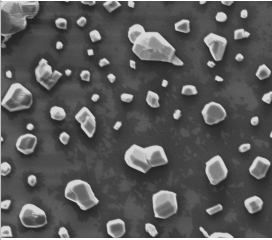
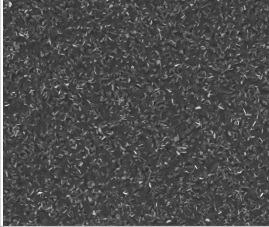
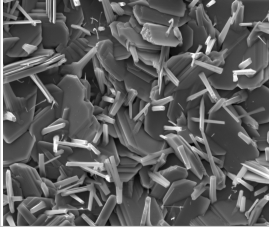
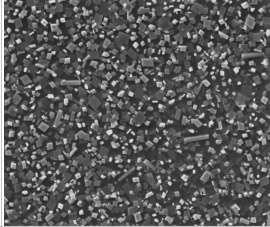
700 Torr				
300 Torr				
0.09 Torr				
	400 °C	500 °C	700 °C	850 °C

Table 2. Scanning electron microscopy (SEM) images obtained from SiO₂/Si samples after deposition of MoS₂ at different pressures and temperatures as listed in the table. The temperatures shown in the table are temperature of SiO₂/Si substrate during deposition. The magnification and the scale bar are the same for all the images.

3.1 Effect of Temperature

In order to determine the optimal condition for the growth of best-quality MoS₂ layers, I investigated, among other parameters, the effect of substrate to source distance. In my initial experiments to grow 2D layered MoS₂, the setup was different from the one I mentioned in Chapter 2. I did not place the substrates on top of the crucible. Instead, I placed them downstream with respect to the crucible making them 2 cm apart from each other. The setup is shown in figure 8. In this setup, the temperature of the substrate is lower than the temperature of the crucible containing MoO₃ precursor. I carried out several (400 °C and 500 °C) experiments with the substrate temperature < 700 °C but none of them showed Raman spectra characteristic of MoS₂. Typical SEM images obtained from such samples are shown in figure 9. Based upon these results, MoS₂ growth at low temperatures (< 700 °C) is not feasible. That is the reason why I changed my experiment setup for the following experiments. I placed the substrates right on top of the crucible, with the expectation that the growth temperature is approximately the same as the MoO₃ temperature.

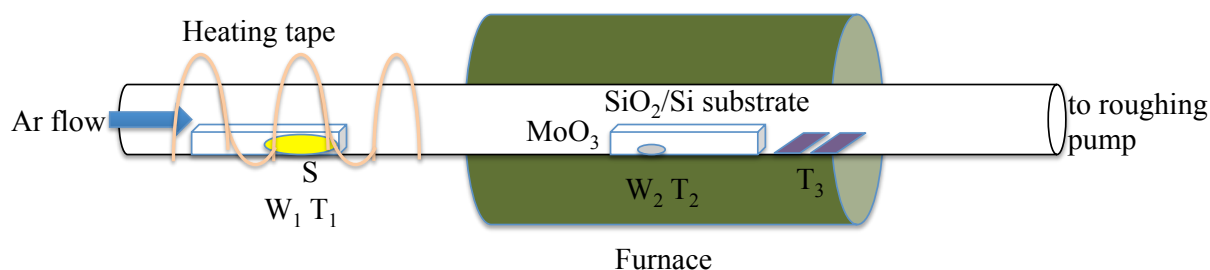


Figure 8. W₁ and T₁ are the weight and temperature, respectively of sulfur. W₂ and T₂ are the weight and temperature, respectively of MoO₃. T₃ is the temperature of SiO₂/Si substrate.

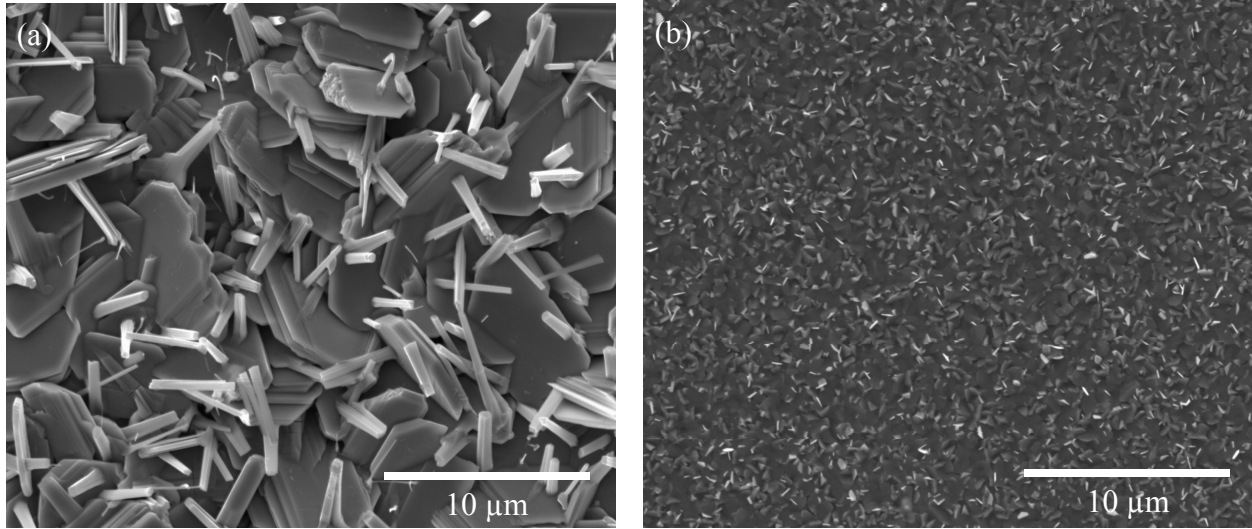


Figure 9. SEM images obtained from SiO₂/Si samples after deposition at temperatures $T_3 =$ (a) 500 °C and (b) 400 °C. Both the depositions were carried out with the total pressure (Ar flowing) maintained at 0.09 Torr. $W_1 = 80$ mg, $T_1 = 85$ -115 °C, $W_2 = 40$ mg, and $T_2 = 700$ °C.

3.2 Effect of Precursor Pressure and Flow Rate

All of my initial experiments were carried out using a constant Ar flow rate of 15 sccm at low pressure (0.09 Torr) using the CVD system reported in Chapter 2. I used 30 mg of MoO₃ in the center crucible and 80 mg of sulfur in the upstream crucible as the precursors. (The amount of precursors used in these low-pressure experiments are more than those used in the high-pressure (~ 1 atm) experiments. This is because the loss of precursors via vapor transport is higher when the chamber pressure is lower than when it is maintained at higher pressures.) It took approximately 18.5 minutes to heat the center crucible to 700 °C. After the center crucible reached 700 °C, I heat sulfur source with a heating tape. The sulfur temperature during

MoS₂ growth was not very stable. It was fluctuating between 85 °C and 115 °C. The temperature of center crucible was held at 700 °C for 15 mins after which both the furnace and heating tape were turned off. The results of these growth experiments are shown in figure 10.

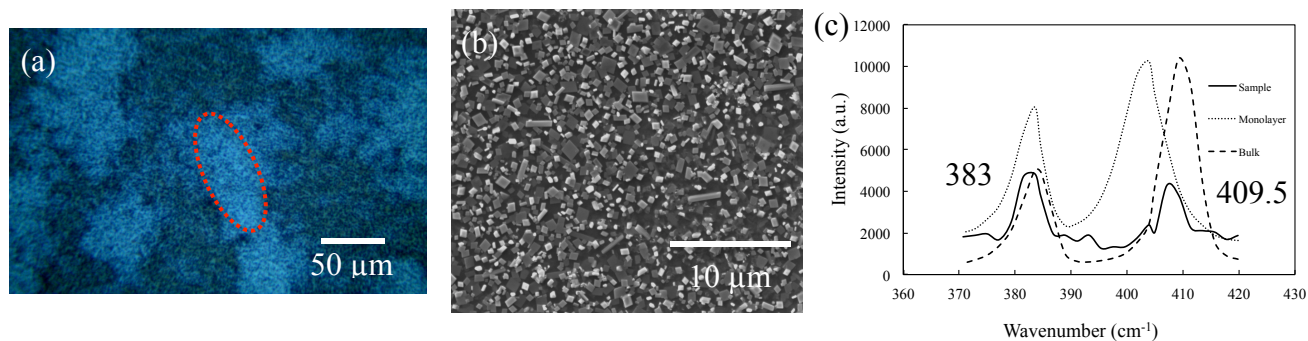


Figure 10. (a) Optical microscopy images, (b) SEM image, and (c) Raman spectrum obtained using a laser wavelength $\lambda = 785$ nm and power = 1 mW from a SiO₂/Si sample after deposition at 0.09 Torr. $T_1 = 85$ -115 °C, $W_1 = 80$ mg, $T_2 = 700$ °C, and $W_2 = 30$ mg.

Figure 10(a) is a typical optical microscopy image obtained from the sample. The color variation visible in the image are due to the composition contrast. The brighter and the darker regions correspond to MoS₂ and non-MoS₂, respectively. An SEM image of the sample is shown in figure 10(b). We can see many cubic and cuboid structures in the SEM image. However, the presence of MoS₂ layers is not clear. Figure 10(c) shows the Raman spectrum obtained from the sample inside the red dotted oval in figure 10(a). The dashed and dotted lines in the plot correspond to bulk and monolayer MoS₂, respectively. The two stronger intensity Raman peaks observed at 383 cm⁻¹ and 409.5 cm⁻¹ indicate the presence of bulk-like MoS₂ on this sample. I have conducted other experiments with different precursor amount (20 mg MoO₃) and also with

sulfur heated when center crucible is at 600 °C or 650 °C. However, none of the samples yielded MoS₂ signal in Raman spectroscopy measurements. The reproducibility was not very good and I did not find any thin layered MoS₂ on the sample. I conclude that low pressure (0.09 Torr) is not ideal for 2D layered MoS₂ growth.

After a series of growth experiments at low pressure, I investigated the effect of increasing the total pressure in the CVD reactor on the growth morphologies. I ramped up the chamber pressure by closing the valve connected to the roughing pump and introducing Ar flow (10, 100, 150, 200 sccm) into the chamber for 30 or 60 mins before vaporizing the precursors. The growth pressure was set at 100, 300 or 700 Torr in different experiments. Since the vaporization of precursors in high pressure (> 100 Torr) environment is not as easy as in low pressure environment. It is because the loss of precursors via vapor transport is higher when the chamber pressure is lower than when it is maintained at higher pressures. The temperature (T_2) of center crucible was set at

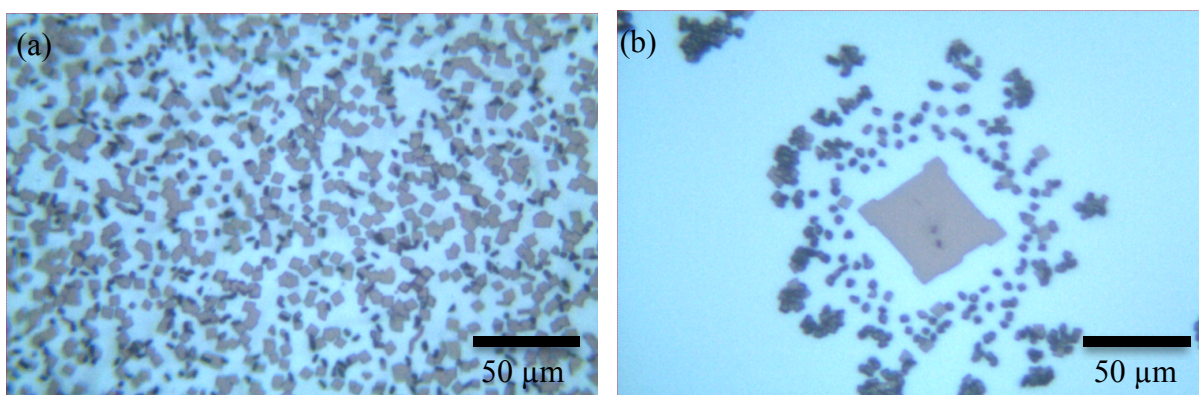


Figure 11. (a) and (b) are optical microscopy images obtained from a SiO₂/Si sample in different regions after deposition carried out using 100 Torr, $T_1 = 110-140$ °C, $W_1 = 80$ mg, $T_2 = 750$ °C, and $W_2 = 20$ mg.

750 °C or 850 °C and the temperature (T_1) of upstream crucible was set at 120 °C or 200 °C correspondingly. (T_1, T_2) = (120 °C, 750 °C) and (200 °C, 850 °C). The amount of sulfur was 80, 100, or 120 mg and the amount of MoO_3 was 20, 15, 10, or 8 mg in different experimental setups.

Figure 11 shows typical optical micrographs from the samples grown using 80 mg sulfur and 20 mg MoO_3 as precursors with the pressure at 100 Torr and $T_2 = 750$ °C. We can see light blue SiO_2 in the background and cubic non- MoS_2 structures from different regions of the sample. These samples did not show any MoS_2 signal. The first successful sample with triangle-shaped MoS_2 was obtained at 300 Torr with 100 sccm Ar flow rate at 850 °C. The optical micrograph, Raman spectrum, and SEM images acquired from this sample are shown in figures 12 and 13.

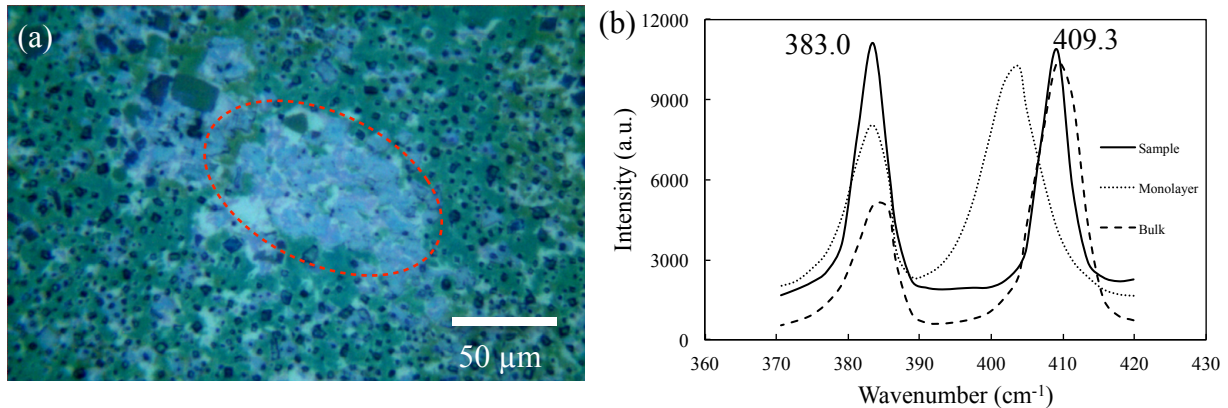


Figure 12. (a) Optical microscopy image and (b) Raman spectrum obtained from the elliptical region highlighted by a red dashed line in (a) corresponds to bulk MoS_2 . SiO_2/Si sample after deposition carried out at 300 Torr, $T_1 = 200$ °C, $W_1 = 80$ mg, $T_2 = 850$ °C, and $W_2 = 20$ mg.

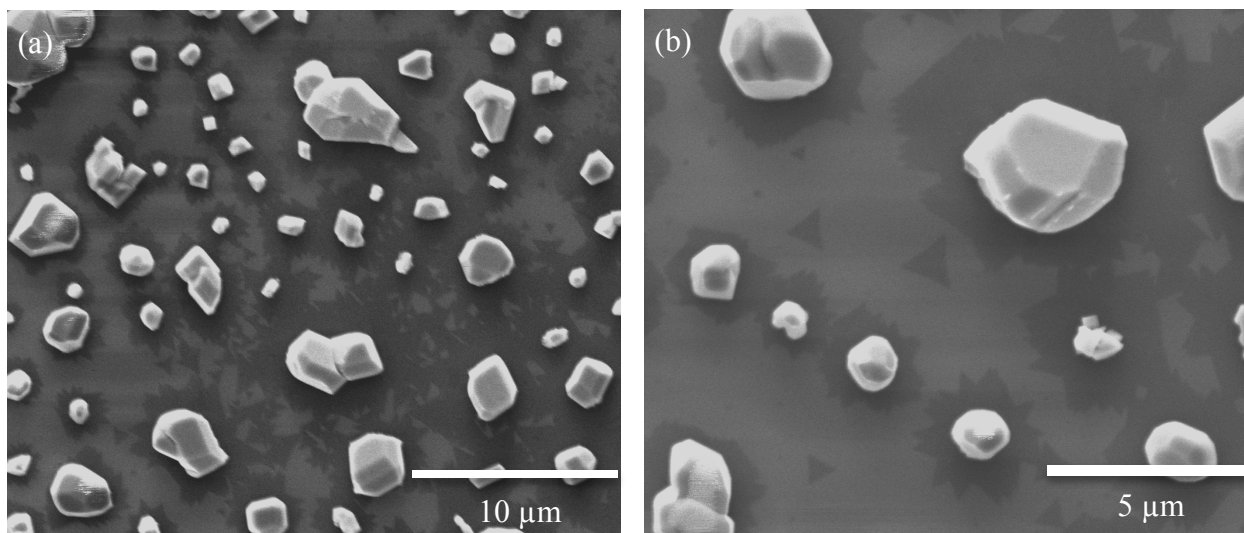


Figure 13. SEM images obtained from SiO₂/Si sample same as in figure 12. (a) and (b) are from different areas and at different magnification. Darker contrast triangles were first discovered around the 3D particles. The triangles are MoS₂ and 3D particles are probably unreacted MoO₃ or partially reduced MoO_{3-x}S_x.

Figures 13(a) and (b) are two representative SEM images obtained from the same sample shown in figure 12. As we can see in figure 13, there are many sub-micrometer scale darker contrast triangles around the brighter contrast particles. These 3D particles are probably unreacted MoO₃ or partially reduced molybdenum oxysulfide (MoO_{3-x}S_x) acting as seeds for MoS₂ triangle growth. In my experiments, I observed these triangular features primarily in those regions of the sample that are in contact with the crucible walls. There are also lots of non-MoS₂ structures at the center part of the sample as shown in figure 14. These initial experiments are promising and indicated that triangular-shaped MoS₂ islands form at these growth conditions. Moreover, the presence of large 3D islands suggest that there is excess MoO₃ precursor and only a portion of which is converted to MoS₂. In order to maximize MoS₂ island growth and eliminate

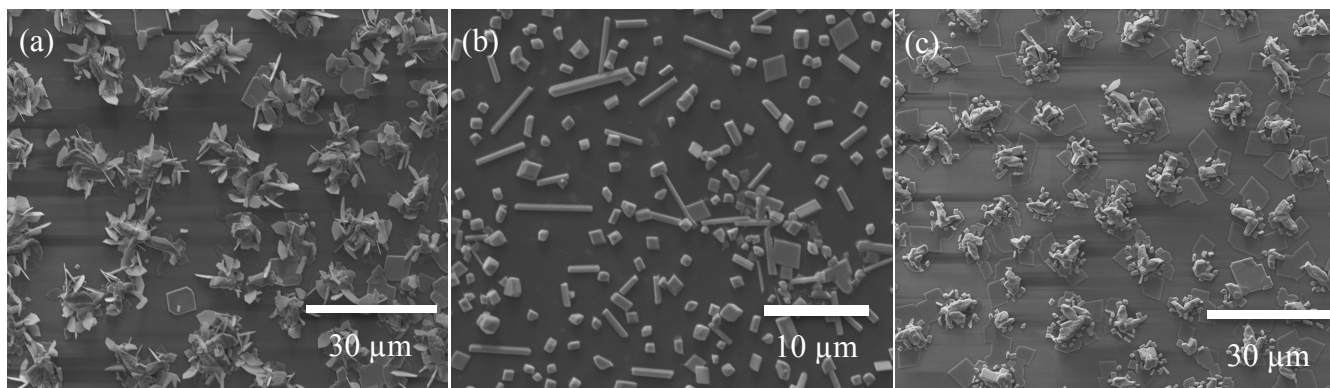


Figure 14. SEM images obtained from the center part of the same SiO_2/Si sample as in figures 12 and 13. (a), (b), and (c) were from different areas of center part of the sample. The larger 3D structures visible in all these images are likely to be MoO_3 or partially reduced $\text{MoO}_{3-x}\text{S}_x$.

MoO_3 precursor from the sample, I have also experimented with reduced amounts of MoO_3 precursor. However, as I will discuss later in this Chapter, complete transformation of MoO_3 to MoS_2 has been challenging.

I have also used much higher pressure (700 Torr) for my experiments. I found that the resulting MoS_2 triangles are much bigger and denser compared to those grown at lower pressures. In my experiments, I observed triangular islands of sizes between 3 μm and 14 μm . Figures 15 and 16 show representative SEM images obtained from the SiO_2/Si samples grown using 700 Torr. On some of the triangles, there are 3D particles situated at their centers (see figure 15). These particles are relatively smaller than those observed in samples grown using lower pressure (see figure 13). Given that the particles appear centrosymmetric with respect to the triangular islands, I speculate that these particles act as "seeds" for the nucleation and growth of MoS_2 triangles. Moreover, there are "tails" at the vertices of the bigger triangles (side length \sim

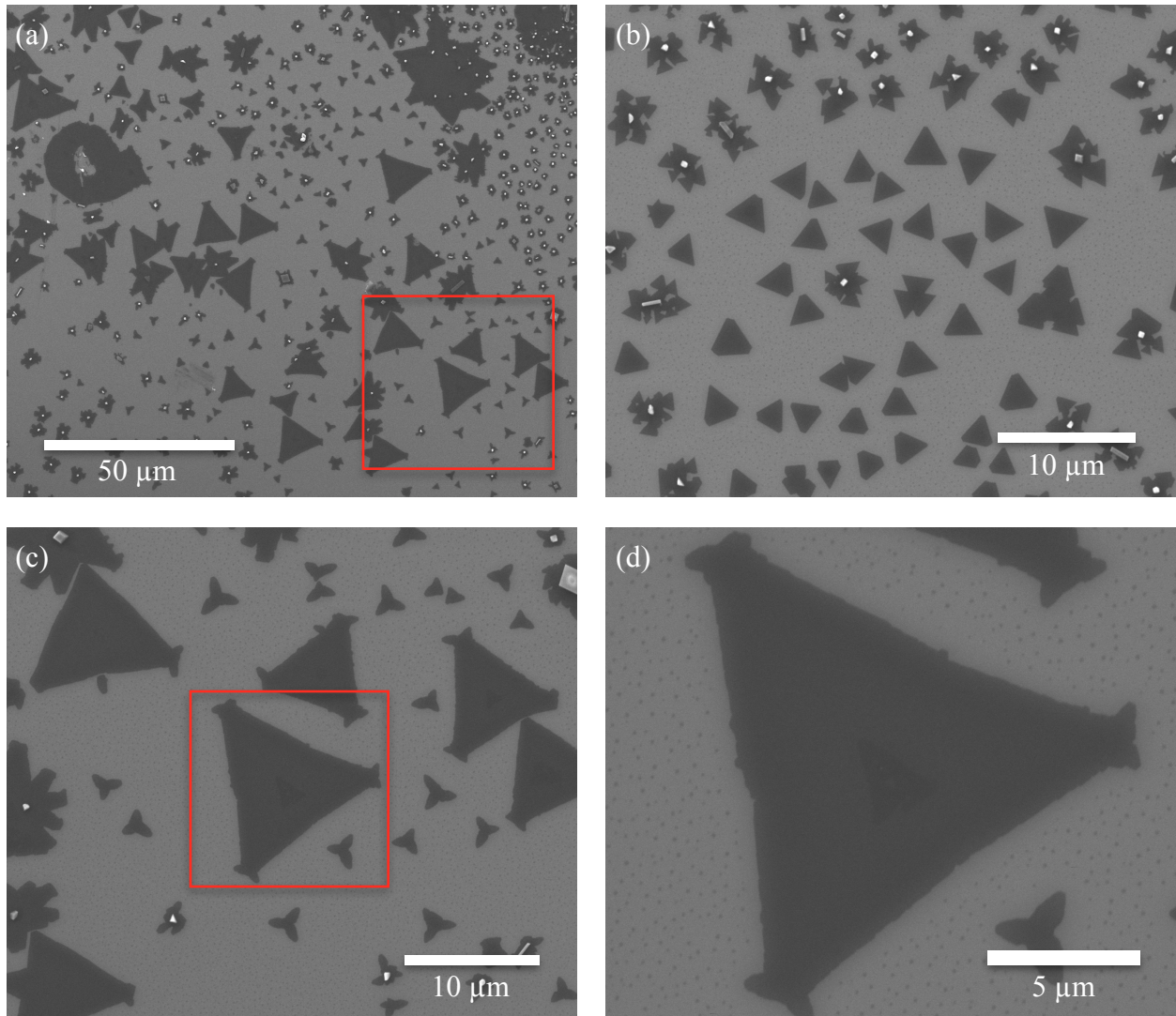


Figure 15. SEM images obtained from a SiO₂/Si sample after the deposition of MoS₂ with the pressure of 700 Torr, T₁ = 200 °C, W₁ = 100 mg, T₂ = 850 °C, and W₂ = 10 mg. (a) Overview of the different island morphologies. (b) Higher magnification images of smaller MoS₂ triangles. (c) and (d): higher magnification images of regions highlighted in (a) and (c), respectively.

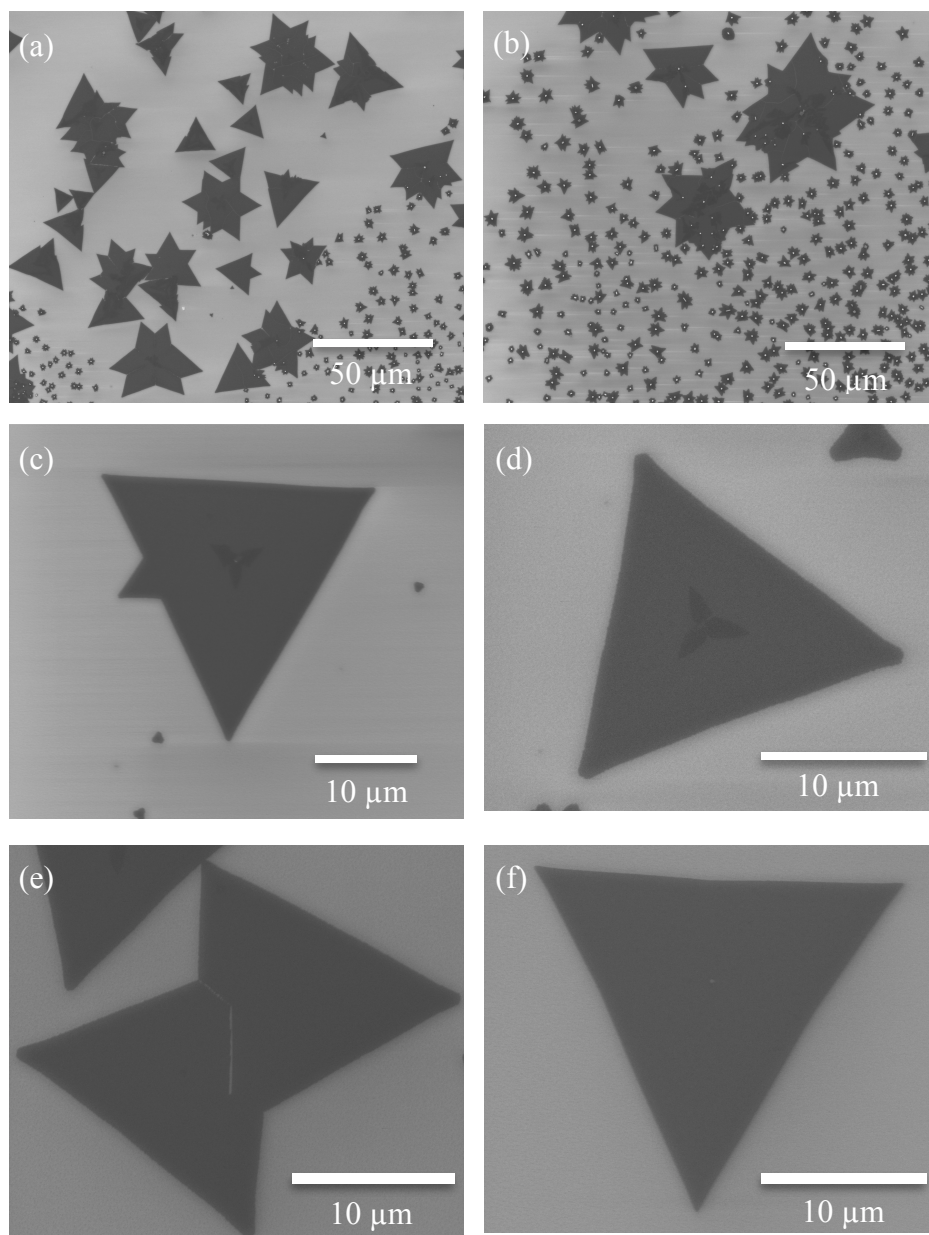


Figure 16. SEM images obtained from a SiO_2/Si sample after the deposition of MoS_2 with 700 Torr, $T_1 = 200\text{ }^\circ\text{C}$, $W_1 = 120\text{ mg}$, $T_2 = 850\text{ }^\circ\text{C}$, and $W_2 = 8\text{ mg}$. (a) and (b) Overview of the different island morphologies. (c) - (f) Higher magnification images of triangles with side length up to $25\text{ }\mu\text{m}$. The star and other regular but non-triangular shapes visible in these images are due to the presence of multiple rotational domains within the islands.

20 μm); and smaller islands (side length $\sim 3 \mu\text{m}$) are bounded by concave edges (see figures 15(c) and (d)). Higher magnification SEM images, such as the one in figure 15(d), reveal the presence of numerous smaller islands in the vicinity of larger triangles. Presumably, these are also MoS_2 islands. On the top of a few larger triangles, we have also observed smaller triangles, indicative of bilayer growth (see figures 15 and 16). In addition to regular equilateral triangular shapes, the images also reveal the presence of a variety of shapes, most of which appear to be aggregates of smaller triangles, such as the islands in figure 15(b) and star-shaped islands in figures 16(a) and (b). Such shapes are likely a consequence of rotational domains growing along the existing edges of a parent island. This process is probably best illustrated by the island in figure 16(c), in which a smaller triangle is attached along one of the edges of a larger (parent)

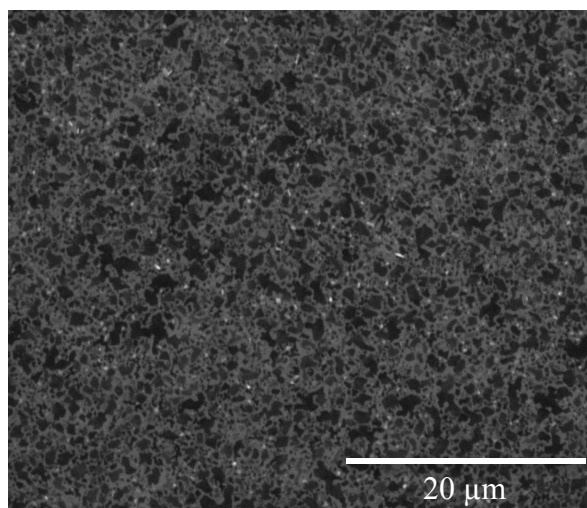


Figure 17. A typical SEM image obtained from SiO_2/Si sample after deposition under 300 Torr, $T_1 = 200 \text{ }^\circ\text{C}$, $W_1 = 80 \text{ mg}$, $T_2 = 700 \text{ }^\circ\text{C}$, and $W_2 = 15 \text{ mg}$.

triangle. Islands with shapes such as those seen in figure 16(e) could form as a result of two domains of different orientations growing into each other. I have also tried growing MoS₂ at lower temperature (700 °C) with the same pressure (300 Torr). Figure 17 is a typical SEM image obtained from a sample grown using 700 °C. The surface morphology of this sample is in distinct contrast to the triangular island morphologies observed on samples grown using higher-temperatures. Raman spectra (not shown) obtained from this sample did not indicate the presence of MoS₂. Based upon all the results presented so far, I conclude that 2D layers of MoS₂ are best grown using high pressures (> 100 Torr) and high temperatures (> 700 °C).

3.3 2D Layered MoS₂ Growth with Different Amounts of Precursors

I have also conducted a series of experiments to study how the amount of precursors influence sample morphology. As mentioned earlier, there are lots of undesired non-MoS₂ structures on the sample and all the MoS₂ triangles were found only at the edges of the sample that are in contact with the crucible walls. In order to maximize the the coverage rate of MoS₂ and eliminate (or minimize) remnant oxides and other non-MoS₂ structures, I experimented with different S/MoO₃ ratios. The rationale behind these experiments is that the fraction of MoS₂ vs. MoO₃ can be increased by increasing the S/MoO₃ ratio.

Figures 18(a-c) summarize the effect of increasing S/MoO₃ ratio on the growth morphologies. At lower S/MoO₃ ratio, there are lots of non-MoS₂ structures (3D cubes and rods) as seen in figure 18(a). With increasing S/MoO₃ ratio, the areal coverage of non-MoS₂ structures is found to be lower and more layered MoS₂ structures are observed (see figures 18(b) and (c)). These results are consistent with my prediction. However, I was not able to eliminate all the non-MoS₂

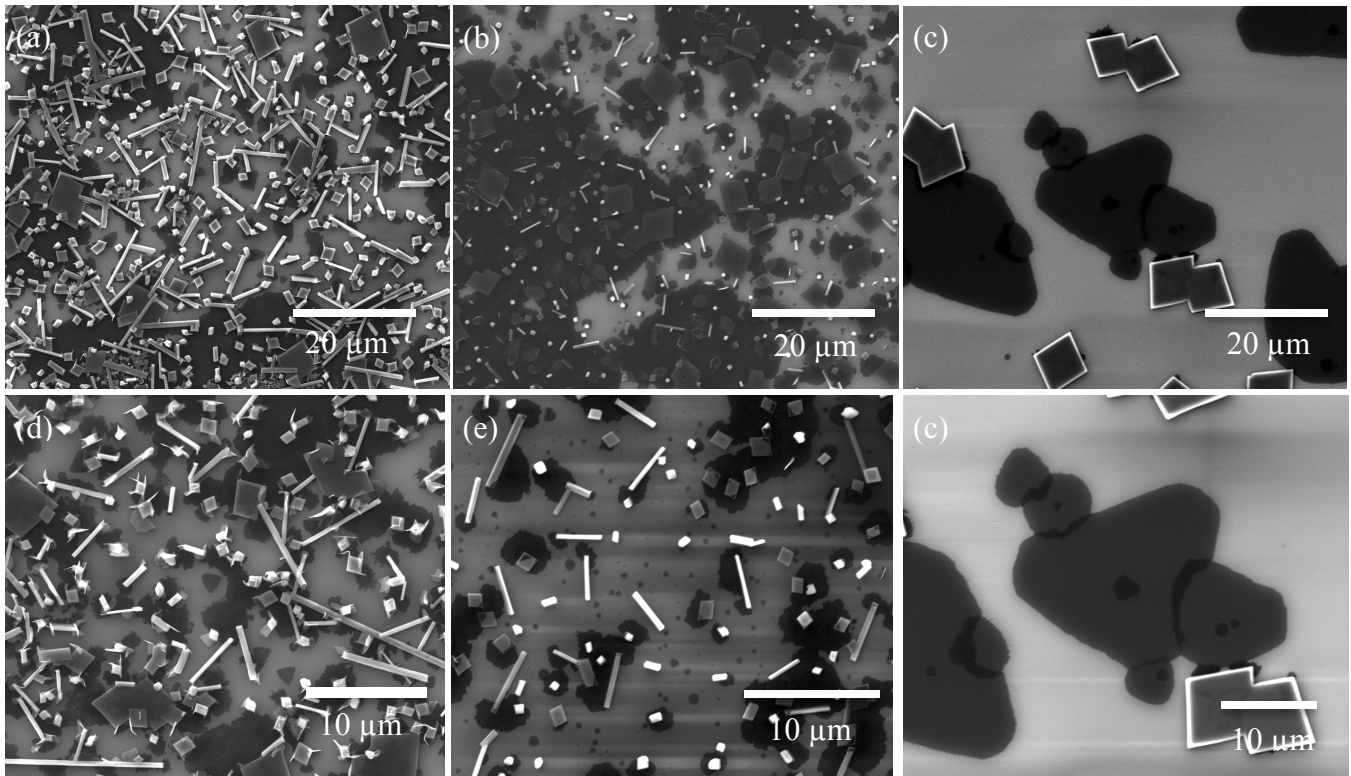


Figure 18. SEM images obtained from a SiO_2/Si sample after the deposition of MoS_2 using 700 Torr, $T_1 = 200\text{ }^\circ\text{C}$, $T_2 = 850\text{ }^\circ\text{C}$, with: (a) $W_1 = 120\text{ mg}$ and $W_2 = 8\text{ mg}$, i.e. $\text{S}/\text{MoO}_3 = 120/8$; (b) $W_1 = 200\text{ mg}$ and $W_2 = 10\text{ mg}$ ($\text{S}/\text{MoO}_3 = 200/10$); and (c) $W_1 = 200\text{ mg}$ and $W_2 = 5\text{ mg}$ ($\text{S}/\text{MoO}_3 = 200/5$). The top and bottom panels show lower and higher magnification images, respectively of the sample.

structures using this approach. Non- MoS_2 structures are observed despite using very small amounts of MoO_3 , i.e. with high S/MoO_3 ratios (200/5) as in figures 18(c) and 19. Moreover, the MoS_2 triangles still are only found at the edges of the sample that are in contact with the crucible walls.

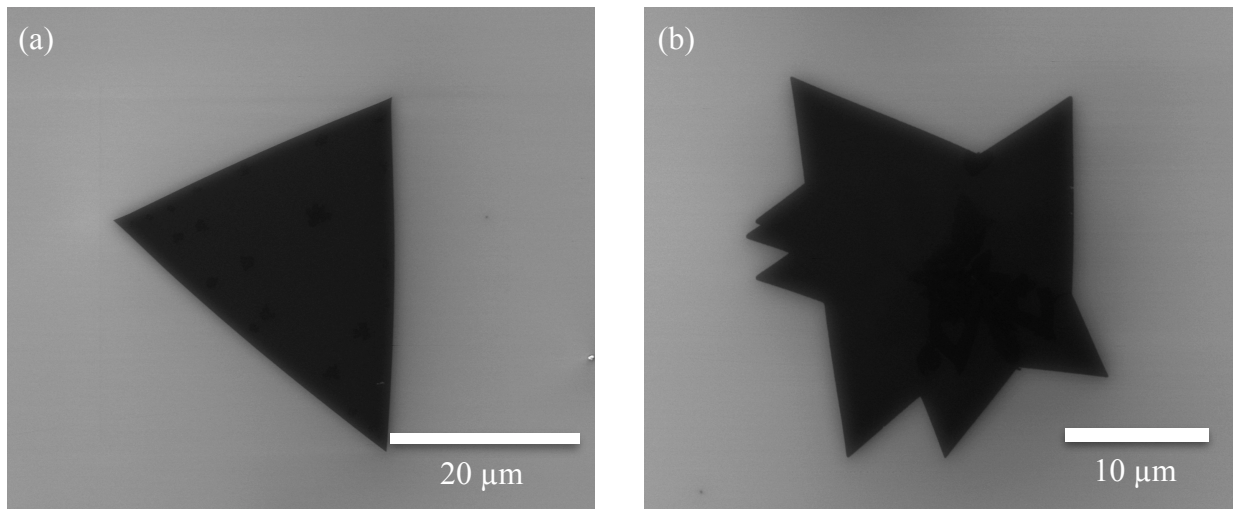


Figure 19. SEM images obtained from SiO₂/Si sample same as from figure 18.

(a) Triangles and (b) stars with side length of 30 μm were found at the edge of the sample.

3.4 Observation of Site-Specific Morphologies

In order to eliminate those non-MoS₂ structures, it is necessary to study the morphology throughout the sample. The thin layered MoS₂ triangles usually appear only in the regions that are in contact with the crucible walls. Thick (micrometer scale) MoS₂, and non-MoS₂ structures usually grow between the two crucible walls. Figures 20(a) to (h) are SEM images illustrating the effect of sample position with respect to the MoO₃ crucible on the resulting growth morphologies. From left to right, i.e. figures 20(a) to (d), the images show morphologies obtained outside the crucible, at the walls, inside the walls, and at the center of the sample. These images along with Raman spectra (not shown) help us better understand the growth kinetics of MoS₂. In my experiments, MoS₂ is barely observed and most abundant outside and inside the crucible, respectively. The desired layered MoS₂ islands are obtained along the edges of the samples that are in contact with the walls of the crucible. Based upon these observations, I

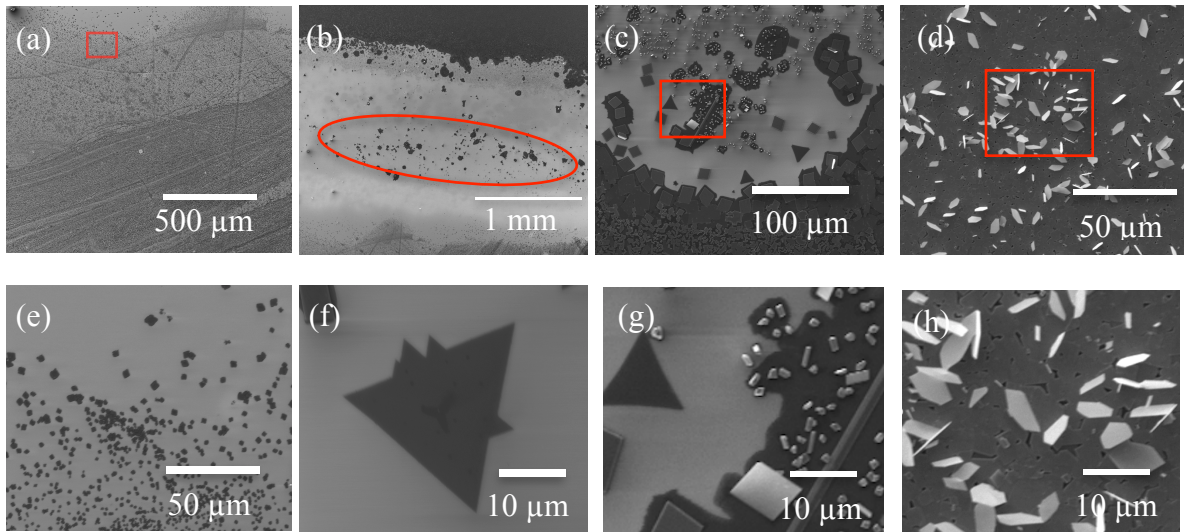


Figure 20. SEM images obtained from a SiO_2/Si sample after deposition using 300 Torr, $T_1 = 200\text{ }^\circ\text{C}$, $W_1 = 80\text{ mg}$, $T_2 = 850\text{ }^\circ\text{C}$, and $W_2 = 4\text{ mg}$. Images (a)-(d) are obtained from the sample at a region (a) farthest from the sample center and outside the walls of the crucible, (b) in contact with the walls, (c) near the inside edges of the walls, and (d) closer to the center of the sample. The top and bottom panels show lower and higher magnification images of the regions highlighted in the overview image and in the top panel images, respectively. (e)-(h) are magnified images from highlighted area in (a)-(e) respectively. (a) Not any MoS_2 observed in this region. (b) A strip of triangles are located along the line in contact with the crucible wall shown in the highlighted area. (c) 3D brighter contrast particles appear in this region. (d) Thick (micrometer scale) non- MoS_2 material covers the whole substrate with brighter contrast structures standing on top.

propose the following: MoS₂ layer formation requires appropriate fluxes of both MoO₃ and S. Outside the crucible, MoO₃ vapor flux is limited probably due to blocking by the crucible walls and hence there is little opportunity for MoO₃ to react with S and form MoS₂. As a consequence, growth of MoS₂ is suppressed in this region (see figure 20(a)). In contrast, the flux of MoO₃ vapor is highest at the center of the sample and this results in the deposition of a thick film of MoS₂ and partially sulfurized MoOS₂ (see figure 20(d)). Along the edges in contact with the crucible, it seems that the fluxes of MoO₃ and sulfur are most favorable for the growth of layered MoS₂, as visible in figure 20(b).

3.5 Two-Step 2D Layered MoS₂ Growth

The mechanisms underlying the CVD of 2D MoS₂ layers are not yet well established. Very little is known concerning the diffusional and reaction processes occurring during the growth of MoS₂ from MoO₃. From my experimental results presented in the previous sections, it is clear that the growth of MoS₂ in my system depends on multiple parameters (relative fluxes of S and MoO₃, substrate temperature, operating pressure, etc.). Moreover, the flux of MoO₃ and substrate temperature are coupled because they both depend on the temperature of the alumina boat; increasing the substrate temperature will automatically lead to higher MoO₃ flux. As a means to independently control these two parameters and hence gain new insights into this MoO₃ → MoS₂ transformation, I carried out two-step growth experiments as follows: first, I deposit a thin film of MoO₃; in the second step, sulfur is vapor transported to the MoO₃-covered surface to initiate MoS₂ growth. The details of these experiments are presented below.

First, I placed only the crucible with MoO₃ (5 mg) and SiO₂/Si substrate in the reactor with the

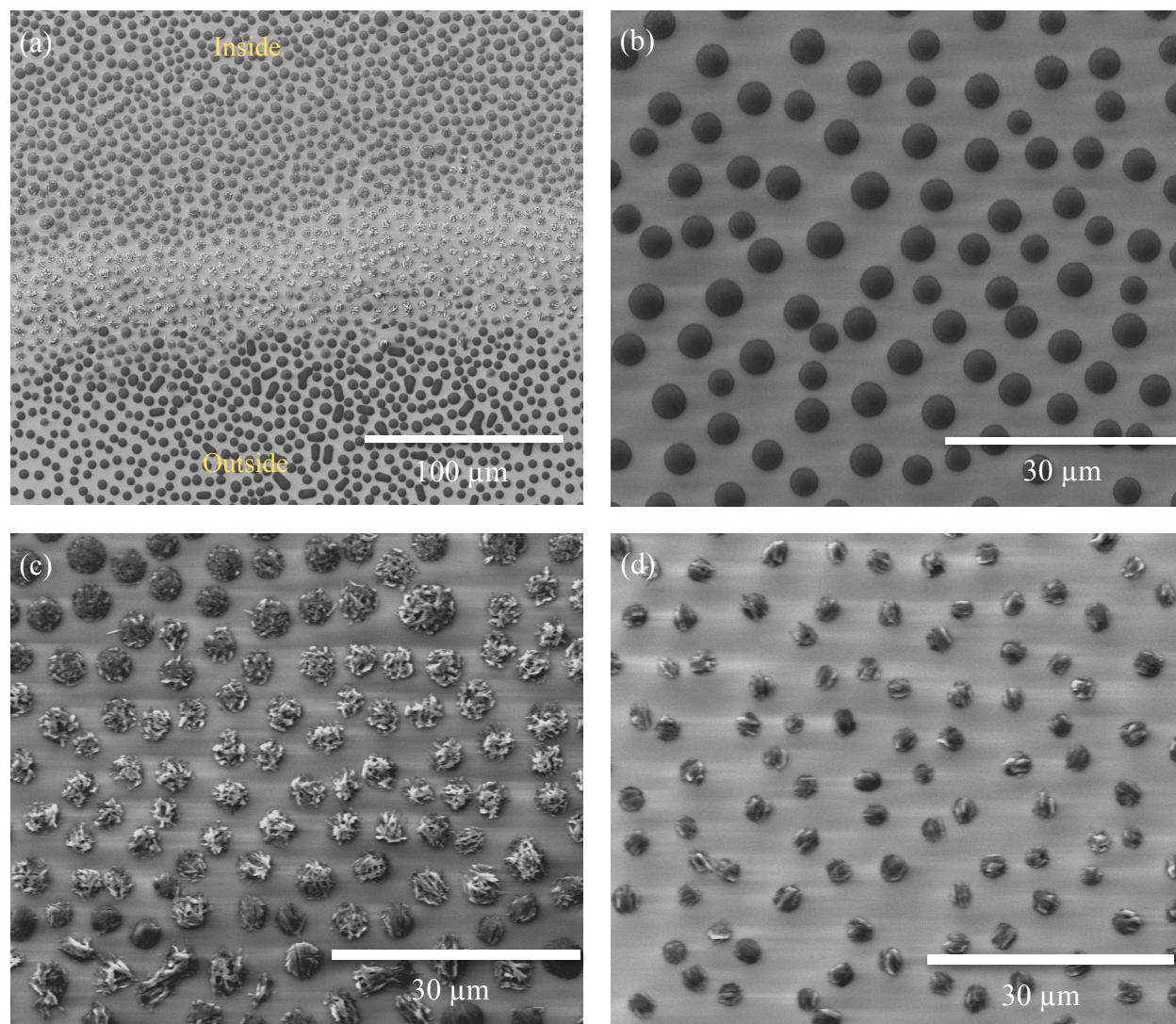


Figure 21. Typical SEM images obtained from a SiO₂/Si sample after deposition of 5 mg MoO₃ under 180 Torr at 850 °C. (a) Overview of the MoO₃ deposited regions surrounding the crucible walls. (b-d) Morphologies and areal coverages of 3D MoO₃ mounds observed on the region of the sample is (b) outside the crucible, (c) along with edges in contact with the crucible, and (d) inside the crucible.

substrate positioned right on top of the crucible. I ramped up the pressure with 50 sccm Ar flow to 115 Torr over the course of an hour. Similar to my previous experiments, the temperature for

MoO₃ deposition was set at 850 °C. After staying at 850 °C under 180 Torr (Ar + MoO₃ vapor + sulfur vapor) for 10 mins, I switched off the furnace, purged the system of all remaining precursors, and let the system cool to room temperature in air. Surprisingly, the as-deposited MoO₃ was not in thin film form but the substrate surface was covered with 3D hemispherical mounds (~ 3 μm in diameter). Majority of the mounds appear smooth (see figure 21(b)) while others exhibit rough and/or spiky morphologies as seen in figures 21(c)-(d). It appears that the morphologies of these mounds depend on the position of the sample with respect to the crucible. Irrespective of their shape, all these mounds are evenly distributed on the substrate.

After the MoO₃ deposition and SEM analysis, I put the sample back in the reactor and exposed it to sulfur vapor at high temperatures. I placed 80 mg of sulfur in the upstream crucible and the substrate on top of another crucible at the hottest zone of the tube. The sulfurization was carried out at 850 °C under 200 Torr of Ar flowing at 200 sccm over a period of 10 mins. These parameters are similar as those used to grow the sample shown in figure 20. The results of this two-step growth are very promising. I obtained highly dense arrays of MoS₂ triangles in the vicinity of the edges of the sample that are in contact with the crucible, as shown in figure 22. Figure 23 is a plot of the Raman spectra obtained from this region of this sample. By comparing the peak positions with those of monolayer, bilayer, and bulk MoS₂, I find that the triangles growing in the regions surrounding the crucible walls are monolayer and bilayer MoS₂. The areal coverage of MoS₂ triangles was higher than the coverages typically observed in my one-step growth experiments. I find that the number density of MoO₃ mounds is comparable to that of the MoS₂ triangles based upon which, I speculate that each of the MoO₃ mounds transforms into one MoS₂ triangle. Moreover, the non-MoS₂ structures, commonly observed in the one-step CVD

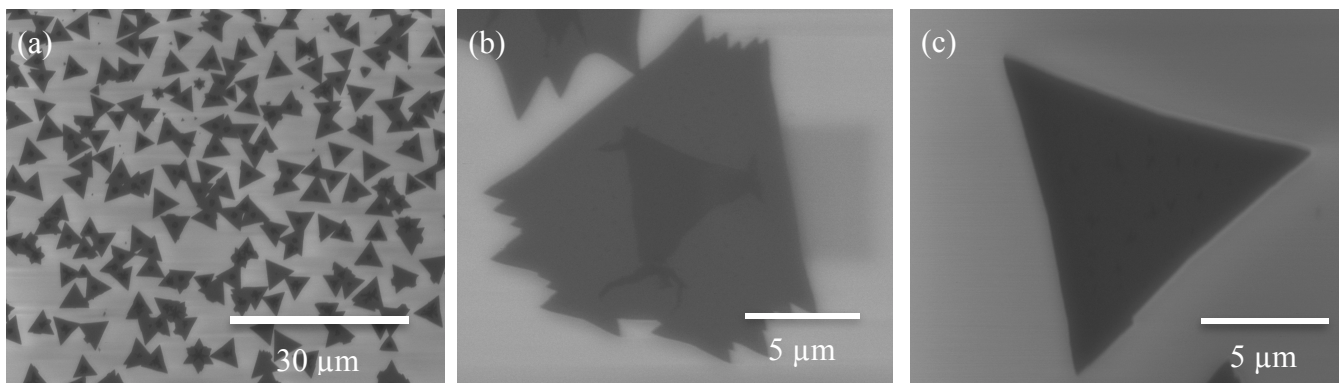


Figure 22. Representative SEM images obtained from a SiO₂/Si sample after sulfurization of MoO₃-covered substrate with 80 mg sulfur at 850 °C under 200 Torr. (a) Highly dense arrays of MoS₂ triangles distributed evenly along and around the edges that are in contact with the crucible walls. (b) and (c) Higher magnification images of few-layered MoS₂ islands with faceted edges.

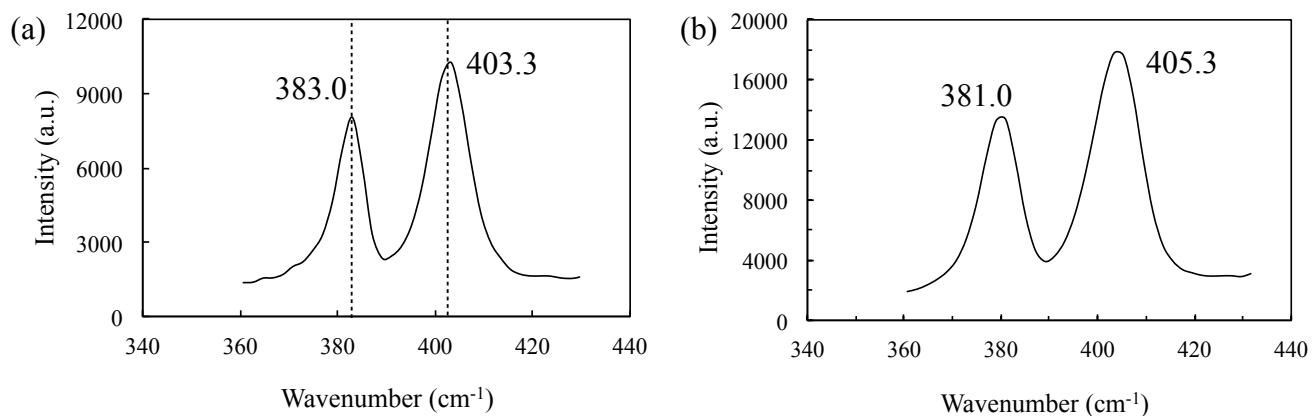


Figure 23. Raman spectra obtained from a SiO₂/Si sample same as from figure 22. (a) Monolayer MoS₂ triangle from the region in figure 22(c). The dotted lines represent the peak positions for monolayer MoS₂. (b) 2 monolayers MoS₂ triangle from the region in figure 22(b).

process, are virtually non-existent in this two-step growth approach. Away from the edges, near the center of the sample, I obtained thick MoS₂ (> 5 layers) islands (see figure 24). Figure 25(a) shows Raman spectra obtained from the regions near the center of the sample. The peak positions are comparable to those expected for bulk MoS₂, indicating that the layers are thick (> 5 layers). Raman spectra (see figure 25(b)) obtained from the regions inside the crucible reveal the formation of multi-layered MoS₂ (2~5 layers). This result is in striking contrast with the non-MoS₂ structures (and partially sulfurized features) that I typically observe at the center parts of the samples grown using one-step process. All of these results are very encouraging and the two-step approach seems to be a promising route to grow high-quality layered MoS₂ over large areas.

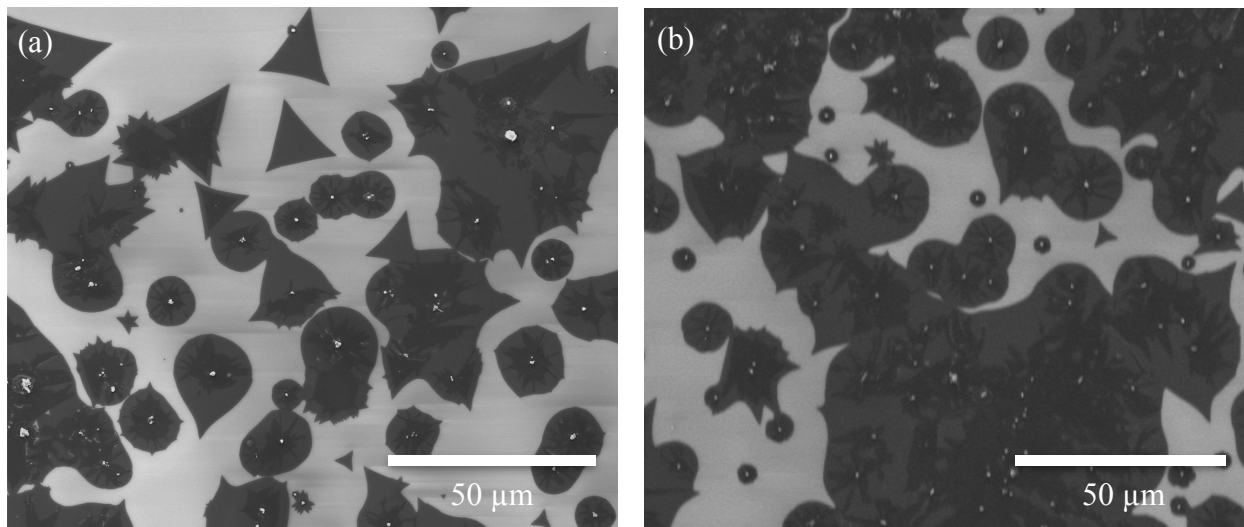


Figure 24. SEM images obtained from the same sample as in figure 22. (a) and (b) Morphologies of multi-layered MoS₂ islands obtained at regions (a) inside the crucible walls and (b) closer to the center of the crucible.

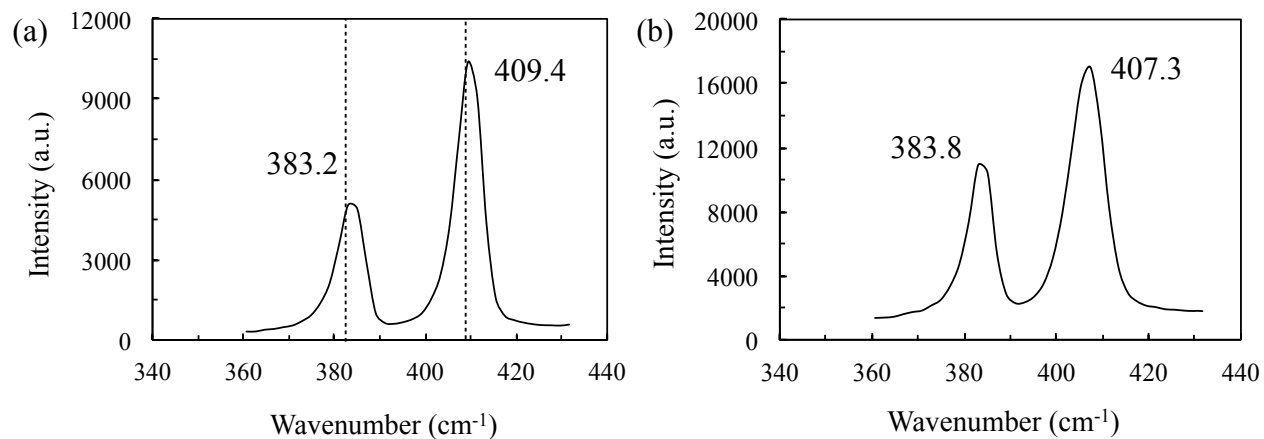


Figure 25. Raman spectra obtained from a SiO₂/Si sample same as from figure 24. (a) Bulk MoS₂ from the region in figure 24(b). The dotted lines represent the peak positions for bulk MoS₂. (b) 4 monolayers MoS₂ from the region in figure 24(a).

In order to make sure that the observed MoS₂ triangles are indeed monolayers, I have also used AFM and determined the surface heights of the triangles. Figure 26 shows AFM images and surface height profiles obtained from a typical triangle-shaped MoS₂ island observed on a SiO₂/Si sample grown using the conditions presented in figure 22. Figure 26(a) shows the surface topography of the island with darker and brighter contrasts corresponding to lower and higher surface heights with respect to the background. At the center of this triangle, there is a smaller triangle rotated 180 degrees with respect to the bottom island. This particular island image was obtained from a sample that has been air exposed for over 120 days. The bright white features, ~3-5 nm tall (see figure 26(b)), decorating the step edges of the first and the second layers are likely to be surface oxides formed post-growth upon air exposure. I would like to point out that these are nanometer-scale islands, which were not visible in my SEM images shown earlier. Figure 26(c) and (d) shows surface height profiles of the first and the second layers obtained, respectively along the yellow and red lines shown in figure 26(a). I measure surface heights of 0.61 ± 0.07 nm and 0.74 ± 0.07 nm for the first and the second layers, respectively. In comparison, the expected interlayer spacing in MoS₂ is 0.65 nm. Given the large uncertainties (0.07 nm, whichever is larger) in AFM measurements, I conclude that this particular island is monolayer thick with a second layer situated on top of it. The AFM measurement provides further evidence that the larger MoS₂ triangles seen in SEM images are monolayer thick with smaller bilayers on top of a few of the islands.

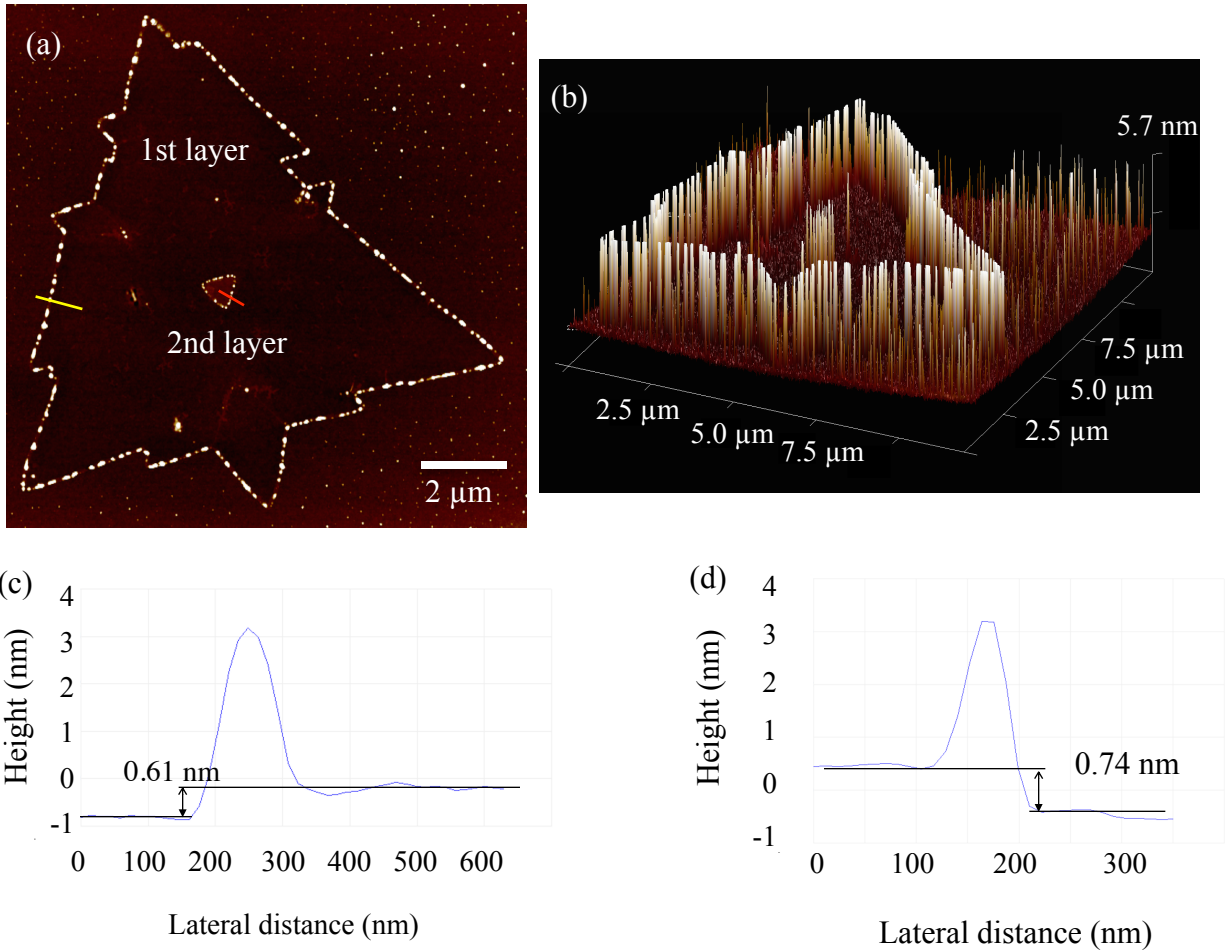


Figure 26. (a) Typical AFM image ($12 \times 12 \mu\text{m}^2$) of a triangular MoS_2 island obtained from a sample shown in figure 22. The brighter and darker contrasts in the image are indicative of higher and lower surface heights. A smaller triangle is observed at the center of this island. (b) 3D perspective image of the island shown in (a). (c) and (d) Surface height profiles obtained along the yellow and red lines shown in (a).

3.6 Discussion

In the previous sections, I have presented a summary of my results obtained from a series of growth experiments carried out as a function of different deposition parameters. Through the low (0.09 Torr) and high pressures (> 300 Torr) experiments, I conclude that 2D layered MoS₂ grows better at higher pressure (> 300 Torr) in my CVD system. These results indicate that a low-pressure environment does not provide sufficient MoO₃ and/or S vapor fluxes required for the growth of MoS₂ layers. I attribute this result to the geometry of my CVD reactor, in which the residence times for the precursors is probably lower at lower pressures and limits the time available for condensation and reaction of the precursors on the growth substrate.

At a given pressure (for example, 300 Torr or higher), I found that higher temperatures (~ 850 °C) is desirable for the growth of layered MoS₂. At lower temperatures (700 °C), the oxide to sulfide transformation was not complete and the samples typically non-layered morphologies and partially sulfurized structures. I attribute these results to a combination of: 1) slower rates of MoO₃ --> MoS₂ conversion and 2) lower rate of MoO₃ desorption from the substrate surface at lower temperatures.

I have successfully demonstrated the growth of layered 2D MoS₂ islands using the one-step CVD process, where the precursors MoO₃ and S are simultaneously introduced, allowed to react, and form MoS₂. In my CVD reactor, I achieved the best results using high pressures (> 300 Torr), high temperatures (~ 850 °C), and high S/MoO₃ precursor ratios. However, I have not been able to completely eliminate the presence of non-MoS₂ (oxides and oxysulfides) on the surface. I attribute this result to limited control over the partial pressures of the precursors in my system. For example, as I mentioned earlier, the temperatures of the substrate and the MoO₃

source are controlled by the same heater and hence the MoO_3 vapor flux increases with increasing substrate temperature. In order to overcome this limitation, I developed a two-step CVD process, where I first deposit MoO_3 and then expose the sample to sulfur vapor. With only MoO_3 in the reactor in the first step, it is easier to control the thickness and uniformity of MoO_3 deposited on the sample, which in turn control the quality of MoS_2 . This two-step growth method looks promising; however, there are still a few challenges. The coverage of MoS_2 is not uniform across the sample; monolayer and bilayer thick MoS_2 islands are obtained along the edges of the crucible while thicker films are found at the center of the sample. These thickness variations are likely due to the shape of the crucible which makes the precursors accumulate near the center part of sample. Additional experiments and detailed characterization of the sample before and after the growths of both MoO_3 and MoS_2 are necessary to determine the role of MoO_3 thickness on the final MoS_2 layer thickness and to determine the factors influencing the thickness uniformity across the sample.

Chapter 4: Conclusion

As mentioned in Chapter 1, monolayer MoS₂ and other two-dimensional layered dichalcogenides have lots of promising applications. All these applications require high quality (phase-pure, stoichiometric, defect-free, and preferably single-domain) monolayer MoS₂. In this work, I investigated the growth of monolayer MoS₂ on SiO₂/Si substrate by chemical vapor deposition. Using MoO₃ and sulfur as the precursors for the CVD of MoS₂ has many benefits as I mentioned in Chapter 2. As part of my thesis, I carried out several growth experiments while varying the deposition parameters such as reactor temperature, reactor pressure, and the starting amount of precursors. The as-grown samples are characterized using optical, scanning electron, and atomic force microscopies and Raman spectroscopy. The results are presented in Chapter 3.

In my experiments, I found that the optimal substrate temperature for the growth of the layered MoS₂ in my system is at 850 °C. At temperatures below 700 °C, I did not observe any MoS₂ growth. Additionally, the pressure in the reactor should be at least 300 Torr to grow monolayer MoS₂. Among all the experiments that I conducted at different temperatures using different amounts of precursors, I have routinely observed MoS₂ growth only at pressures > 300 Torr. Below this value, I obtained non-stoichiometric oxysulfides (MoO_xS_{2-x}). Based upon my studies, I conclude that higher pressure (300 - 700 Torr) is necessary for layered MoS₂ growth.

I have also developed a two-step approach to grow MoS₂ layers. The idea is to deposit MoO₃ of uniform thickness onto SiO₂/Si substrate first and ensure there is no excess MoO₃ in the reactor. Then, I introduce sulfur vapor into the reactor by evaporating the sulfur powder and sulfurize the MoO₃ into MoS₂. With this approach I can control the thickness of MoO₃ and hence MoS₂ film more precisely. Moreover, the sulfurization of MoO₃ into MoS₂ is more complete

based on my experiment results. I have been able to grow MoS₂ over the entire SiO₂/Si substrate. However, additional work is necessary to achieve thickness uniformity over the entire substrate.

The growth temperature in the two-step approach may not be as high as in conventional CVD (850 °C). And, in principle, one can use this two-step approach and grow large-area MoS₂ on SiO₂/Si substrate. However, the fraction of single layer MoS₂ on the substrate still requires improvement. However, additional studies are required to determine the optimal deposition parameters and to demonstrate the large-area growth of high-quality MoS₂ layers of desired thickness. In this regard, I have outlined a few possible future experiments with this new two-step approach. One of the critical factors affecting the MoS₂ layer quality (both thickness and thickness variation across the sample) is the MoO₃ layer thickness and uniformity. The temperature of the MoO₃ source and the substrate and the deposition time all influence the thickness of the MoO₃ thin film. In the second step, probably the important parameters that affect the composition and crystallinity of MoS₂ layers are the sulfur flux and the substrate temperature. I believe that it is possible to grow large-area monolayer MoS₂ in the near future by tuning the thickness of MoO₃ in the first step and the sulfurization temperature during the second step.

Other than growing large area monolayer MoS₂, we can also try to grow lateral and/or vertical heterostructures with different types of 2D layered materials such as graphene, MoSe₂, or WSe₂. The bandgap difference between these 2D materials offers the possibility to create devices with various functionalities. However, this is not a straight-forward task, for example, to grow MoS₂ on graphene. Chemical interactions between MoS₂ and graphene may need to be suppressed to avoid formation of any interfacial compounds. Growth of one chalcogenide over another, as in

MoSe₂ or WS₂ on top of MoS₂, may also be challenging due to intermixing across the interfaces. Growing transition-metal dichalcogenide alloys is another area of research interest. These layers have similar lattice constants (MoS₂: 3.11 Å, MoSe₂: 3.24 Å, WS₂: 3.13 Å); therefore, it is possible to grow substitutional alloys. The optical and electrical properties of these band-gap tunable TMDC alloys allow us to use in future device applications. In conclusion, the future is bright for these two-dimensional layered materials, especially the transition-metal dichalcogenides, which offer a great variety of properties. The recent advances in the development of new device architectures catered to take advantage of the two-dimensional geometries of these material can lead to potentially new applications.

Reference

1. K. S. Novoselov *et al.*, Electric field effect in atomically thin carbon films. *Science* **306**, 666 (Oct 22, 2004).
2. B. Radisavljevic, A. Radenovic, J. Brivio, V. Giacometti, A. Kis, Single-layer MoS₂ transistors. *Nature Nanotechnology* **6**, 147 (Mar, 2011).
3. O. Lopez-Sanchez, D. Lembke, M. Kayci, A. Radenovic, A. Kis, Ultrasensitive photodetectors based on monolayer MoS₂. *Nature Nanotechnology* **8**, 497 (Jul, 2013).
4. M. Bernardi, M. Palumbo, J. C. Grossman, Extraordinary Sunlight Absorption and One Nanometer Thick Photovoltaics Using Two-Dimensional Monolayer Materials. *Nano Letters* **13**, 3664 (Aug, 2013).
5. M. D. Stoller, S. Park, Y. Zhu, J. An, R. S. Ruoff, Graphene-Based Ultracapacitors. *Nano Letters* **8**, 3498 (Oct, 2008).
6. S. Stankovich *et al.*, Graphene-based composite materials. *Nature* **442**, 282 (Jul 20, 2006).
7. H. L. Zhuang, R. G. Hennig, Computational Search for Single-Layer Transition-Metal Dichalcogenide Photocatalysts. *Journal of Physical Chemistry C* **117**, 20440 (Oct 10, 2013).
8. C. Lee, X. Wei, J. W. Kysar, J. Hone, Measurement of the elastic properties and intrinsic strength of monolayer graphene. *Science* **321**, 385 (Jul 18, 2008).

9. C. N. R. Rao, A. K. Sood, K. S. Subrahmanyam, A. Govindaraj, Graphene: The New Two-Dimensional Nanomaterial. *Angewandte Chemie-International Edition* **48**, 7752 (2009, 2009).
10. M. Y. Han, B. Oezylmaz, Y. Zhang, P. Kim, Energy band-gap engineering of graphene nanoribbons. *Physical Review Letters* **98**, (May 18, 2007).
11. C. Ataca, H. Sahin, S. Ciraci, Stable, Single-Layer MX₂ Transition-Metal Oxides and Dichalcogenides in a Honeycomb-Like Structure. *Journal of Physical Chemistry C* **116**, 8983 (Apr 26, 2012).
12. A. Kuc, N. Zibouche, T. Heine, Influence of quantum confinement on the electronic structure of the transition metal sulfide TS₂. *Physical Review B* **83**, (Jun 30, 2011).
13. T. Mang, W. Dresel, *Lubricants and Lubrication* (Feb, 2007)
14. K. F. Mak, C. Lee, J. Hone, J. Shan, T. F. Heinz, Atomically Thin MoS₂: A New Direct-Gap Semiconductor. *Physical Review Letters* **105**, (Sep 24, 2010).
15. A. Splendiani *et al.*, Emerging Photoluminescence in Monolayer MoS₂. *Nano Letters* **10**, 1271 (Apr, 2010).
16. H. Li *et al.*, From Bulk to Monolayer MoS₂: Evolution of Raman Scattering. *Advanced Functional Materials* **22**, 1385 (Apr 10, 2012).
17. K. K. Kam, B. A. Parkinson, DETAILED PHOTOCURRENT SPECTROSCOPY OF THE SEMICONDUCTING GROUP-VI TRANSITION-METAL DICHALCOGENIDES. *Journal of Physical Chemistry* **86**, 463 (1982, 1982).

18. A. J. Grant, T. M. Griffiths, G. D. Pitt, A. D. Yoffe, ELECTRICAL PROPERTIES AND MAGNITUDE OF INDIRECT GAP IN SEMICONDUCTING TRANSITION-METAL DICHALCOGENIDE LAYER CRYSTALS. *Journal of Physics C-Solid State Physics* **8**, L17 (1975, 1975).
19. A. Kumar, P. K. Ahluwalia, Electronic structure of transition metal dichalcogenides monolayers 1H-MX₂ (M = Mo, W; X = S, Se, Te) from ab-initio theory: new direct band gap semiconductors. *European Physical Journal B* **85**, (Jun, 2012).
20. K. E. Dungey, M. D. Curtis, J. E. Penner-Hahn, Structural characterization and thermal stability of MoS₂ intercalation compounds. *Chemistry of Materials* **10**, 2152 (Aug, 1998).
21. R. Kappera *et al.*, Phase-engineered low-resistance contacts for ultrathin MoS₂ transistors. *Nature Materials* **13**, 1128 (Dec, 2014).
22. K. S. Novoselov *et al.*, Two-dimensional gas of massless Dirac fermions in graphene. *Nature* **438**, 197 (Nov 10, 2005).
23. W. Zhou *et al.*, Synthesis of Few-Layer MoS₂ Nanosheet-Coated TiO₂ Nanobelt Heterostructures for Enhanced Photocatalytic Activities. *Small* **9**, 140 (Jan 14, 2013).
24. W. Zhang *et al.*, Ultrahigh-Gain Photodetectors Based on Atomically Thin Graphene-MoS₂ Heterostructures. *Scientific Reports* **4**, (Jan 23, 2014).

25. G.-H. Lee *et al.*, Flexible and Transparent MoS₂ Field-Effect Transistors on Hexagonal Boron Nitride-Graphene Heterostructures. *Acs Nano* **7**, 7931 (Sep, 2013).
26. Q. Xiang, J. Yu, M. Jaroniec, Synergetic Effect of MoS₂ and Graphene as Cocatalysts for Enhanced Photocatalytic H₂ Production Activity of TiO₂ Nanoparticles. *Journal of the American Chemical Society* **134**, 6575 (Apr 18, 2012).
27. Y. Li, Y.-L. Li, C. M. Araujo, W. Luo, R. Ahuja, Single-layer MoS₂ as an efficient photocatalyst. *Catalysis Science & Technology* **3**, 2214 (2013, 2013).
28. W. Lu *et al.*, Functionalized MoS₂ nanosheet-based field-effect biosensor for label-free sensitive detection of cancer marker proteins in solution. *Small* **10**, 1101 (26 March, 2014).
29. D. Sarkar *et al.*, MoS₂ Field-Effect Transistor for Next-Generation Label-Free Biosensors. *Acs Nano* **8**, 3992 (Apr, 2014).
30. J. Xiao *et al.*, Exfoliated MoS₂ Nanocomposite as an Anode Material for Lithium Ion Batteries. *Chemistry of Materials* **22**, 4522 (Aug 24, 2010).
31. C. Liujun *et al.*, Direct Laser-Patterned Micro-Supercapacitors from Paintable MoS₂ Films. *Small* **9**, 2905 (9 Sept., 2013).
32. Y. Hernandez *et al.*, High-yield production of graphene by liquid-phase exfoliation of graphite. *Nature Nanotechnology* **3**, 563 (Sep, 2008).
33. L. M. Viculis, J. J. Mack, R. B. Kaner, A chemical route to carbon nanoscrolls. *Science* **299**, 1361 (Feb 28, 2003).

34. G. H. Chen *et al.*, Preparation and characterization of graphite nanosheets from ultrasonic powdering technique. *Carbon* **42**, 753 (2004, 2004).
35. X. Li, X. Wang, L. Zhang, S. Lee, H. Dai, Chemically derived, ultrasmooth graphene nanoribbon semiconductors. *Science* **319**, 1229 (Feb 29, 2008).
36. Y. Yu *et al.*, Controlled Scalable Synthesis of Uniform, High-Quality Monolayer and Few-layer MoS₂ Films. *Scientific Reports* **3**, (May 21, 2013).
37. J. L. Brito, M. Ilija, P. Hernandez, THERMAL AND REDUCTIVE DECOMPOSITION OF AMMONIUM THIOMOLYBDATES. *Thermochimica Acta* **256**, 325 (Jun 1, 1995).
38. K.-K. Liu *et al.*, Growth of Large-Area and Highly Crystalline MoS₂ Thin Layers on Insulating Substrates. *Nano Letters* **12**, 1538 (Mar, 2012).
39. Y. Zhan, Z. Liu, S. Najmaei, P. M. Ajayan, J. Lou, Large-Area Vapor-Phase Growth and Characterization of MoS₂ Atomic Layers on a SiO₂ Substrate. *Small* **8**, 966 (Apr 10, 2012).
40. X. Ma, M. Shi, Thermal Evaporation Deposition of Few-layer MoS₂ Films. *Nano-Micro Letters* **5**, 135 (2013, 2013).
41. J. Tao *et al.*, Growth of wafer-scale MoS₂ monolayer by magnetron sputtering. *Nanoscale* **7**, 2497 (2015, 2015).
42. J. Djamil, S. Segler, A. Dabrowski, W. Bensch, The influence of carbon content on the structure and properties of MoS_xC_y photocatalysts for light-driven hydrogen generation. *Dalton Transactions* **6**, 1287 (Oct, 2012)
43. Luxel Corporation, Vapor pressure chart.

44. S. Najmaei *et al.*, Vapour phase growth and grain boundary structure of molybdenum disulphide atomic layers. *Nature Materials* **12**, 754 (Aug, 2013).
45. S. Wang *et al.*, Shape Evolution of Monolayer MoS₂ Crystals Grown by Chemical Vapor Deposition. *Chemistry of Materials* **26**, 6371 (Nov 25, 2014).
46. X. Ling *et al.*, Role of the Seeding Promoter in MoS₂ Growth by Chemical Vapor Deposition. *Nano Letters* **14**, 464 (Feb, 2014).
47. L. Brewer, R. H. Lamoreaux, The Mo-S system (Molybdenum-Sulfur). *Bulletin of Alloy Phase Diagrams* **3**, 93 (Sep, 1980)
48. E. Smith, G. Dent, *Modern Raman Spectroscopy: A Practical Approach*. Modern Raman Spectroscopy: A Practical Approach (2005), pp. 1-210.
49. J. Ferraro, *Introductory Raman Spectroscopy* (Nov, 2002)
50. B&W Tek, Theory of Raman Scattering
51. C. Lee *et al.*, Anomalous Lattice Vibrations of Single- and Few-Layer MoS₂. *Acs Nano* **4**, 2695 (May, 2010).
52. S.-L. Li *et al.*, Quantitative Raman Spectrum and Reliable Thickness Identification for Atomic Layers on Insulating Substrates. *Acs Nano* **6**, 7381 (Aug, 2012).
53. HORIBA, Number of layers of MoS₂ determined using Raman Spectroscopy
54. J. Goldstein, D. E. Newbury, D. C. Joy, *Scanning Electron Microscopy and X-ray Microanalysis*. (Apr. 2007)
55. G. Haugstad, *Atomic Force Microscopy: Understanding Basic Modes and Advanced Applications* (Sep, 2012)